A microscopy-based kinetic analysis of yeast vacuolar protein sorting

Jason C. Casler[1] and Benjamin S. Glick[1,2]

1 Department of Molecular Genetics and Cell Biology
University of Chicago
920 East 58th St.
Chicago, IL 60615
USA

2 Corresponding Author
bsglick@uchicago.edu
Tel. 773-202-5315

Abstract

The yeast *Saccharomyces cerevisiae* is amenable to studying membrane traffic by live-cell fluorescence microscopy. We used this system to explore two aspects of cargo protein traffic through prevacuolar endosome (PVE) compartments to the vacuole. First, at what point during Golgi maturation does a biosynthetic vacuolar cargo depart from the maturing cisternae? To address this question, we modified a regulatable fluorescent secretory cargo by adding a vacuolar targeting signal. Traffic of the vacuolar cargo requires the GGA clathrin adaptors, which arrive during the early-to-late Golgi transition. Accordingly, the vacuolar cargo begins to exit the Golgi near the midpoint of maturation, significantly before exit of a secretory cargo. Second, how are cargoes delivered from PVE compartments to the vacuole? To address this question, we tracked biosynthetic and endocytic cargoes after they had accumulated in PVE compartments. The results imply that stable PVE compartments repeatedly deliver material to the vacuole by a kiss-and-run mechanism.

Introduction

Budding yeast has been instrumental for defining mechanisms of membrane traffic. Genetic screens of *Saccharomyces cerevisiae* have identified many conserved components of the biosynthetic and endocytic machineries (Novick et al., 1980; Kaiser et al., 1997). In addition, 4D (time-lapse 3D) fluorescence microscopy of *S. cerevisiae* has been powerful for characterizing membrane traffic pathways (Kurokawa et al., 2013; Day et al., 2016). Unlike most eukaryotes, *S. cerevisiae* has a non-stacked Golgi in which individual cisternae are optically resolvable by fluorescence microscopy (Preuss et al., 1992; Wooding and Pelham, 1998). This property enabled the first direct visualization of Golgi cisternal maturation (Losev et al., 2006; Matsuura-Tokita et al., 2006) as well as later studies of how maturation is regulated by GTPases and vesicle coat proteins (Rivera-Molina and Novick, 2009; Suda et al., 2013; Papanikou et al., 2015; Ishii et al., 2016; Kim et al., 2016; Thomas and Fromme, 2020).

Observations of the yeast Golgi can be synthesized in the following scheme (Pantazopoulou and Glick, 2019). New Golgi cisternae arise at ER exit sites and capture biosynthetic cargoes from the ER. These cisternae then mature by recycling resident Golgi proteins to the ER and to younger cisternae. During the early phase of maturation, one set of resident Golgi membrane proteins recycles with the aid of the COPI vesicle coat, whereas during the late phase of maturation, another set of resident Golgi membrane proteins recycles with the aid of the AP-1 clathrin adaptor. Biosynthetic cargoes are present in the cisternae throughout the maturation process (Casler et al., 2019; Kurokawa et al., 2019). Finally, the terminally mature Golgi cisternae fragment into secretory vesicles.

Recently, we extended this analysis by examining the *S. cerevisiae* endocytic pathway. The evidence suggests that *S. cerevisiae* has a minimal endomembrane system in which the late Golgi, also known as the *trans*-Golgi network (TGN), plays an additional role as an early and recycling endosome (Day et al., 2018). According to this view, yeast cells have two types of endosomes: (a) the late Golgi/TGN, and (b) prevacuolar endosome (PVE) compartments that are typically attached to the vacuole. The PVE compartments are multivesicular bodies reminiscent of mammalian late endosomes (Pelham, 2002; Ma and Burd, 2020).

4D microscopy can also enhance our understanding of cargo delivery to the vacuole. Such experiments require a way to visualize the transport of a biosynthetic vacuolar cargo in live yeast cells. To this end, we built on our recent engineering of a regulatable fluorescent secretory cargo (Casler and Glick, 2019; Casler et al., 2019). A tetrameric red fluorescent protein is fused to an improved dimerizing variant of the FK506-binding protein FKBP, and this construct is targeted to the ER lumen to generate aggregates, which are then solubilized with a ligand to create a fluorescent cargo wave that passes through the Golgi. We have now modified this construct by appending a tetrapeptide vacuolar targeting signal from the precursor to carboxypeptidase Y (CPY) (Valls et al., 1990). This targeting signal is recognized in the Golgi by the Vps10 cargo receptor (Marcusson et al., 1994), which in turn is packaged, with the aid of the GGA adaptors Gga1 and Gga2, into clathrin-coated vesicles destined for PVE compartments (reviewed in Myers and Payne, 2013). The result is that we have a regulatable fluorescent biosynthetic vacuolar cargo, which can be tracked as it moves from the ER through the Golgi to PVE compartments and then to the vacuole.

Our analysis extends prior results from other methods, which revealed the existence of traffic pathways for both biosynthetic and endocytic vacuolar cargoes. Biosynthetic vacuolar cargoes initially move from the ER to the Golgi. Some vacuolar membrane proteins traffic directly from the Golgi to the vacuole with the aid of the Golgi-associated AP-3 adaptor complex (Cowles et al., 1997; Odorizzi et al., 1998; Llinares et al., 2015). By contrast, CPY and certain other vacuolar hydrolases first traffic from the Golgi to PVE compartments (Vida et al., 1993; Conibear and Stevens, 1998). The same PVE compartments also contain endocytosed cargoes, such as the methionine permease Mup1, that are en route to the vacuole (Menant et al., 2006). Within PVE compartments, transmembrane cargo proteins such as Mup1 are packaged into intraluminal vesicles that are transferred from the PVE compartments to the vacuole, where the intraluminal vesicles are degraded (MacDonald et al., 2012). While these insights are extensive, the understanding of vacuolar protein sorting remains incomplete. We have focused on two questions.

First, how is traffic from the Golgi to PVE compartments coordinated with cisternal maturation? The conventional view is that biosynthetic cargoes all travel together through the Golgi until reaching a terminal sorting stage (Griffiths and Simons, 1986; De Matteis and Luini, 2008), implying that vacuolar cargoes would remain in a cisterna throughout the maturation process. However, this idea is called into question by studies of GGA dynamics at the Golgi. We have now replicated work from the Payne lab showing that GGAs arrive earlier than AP-1, and at about the same time as Sec7 (Daboussi et al., 2012), an Arf guanine nucleotide exchange factor that is recruited and activated during the early-to-late Golgi transition (Losev et al., 2006; McDonold and Fromme, 2014). In addition, as described below, we have now tracked the passage of a fluorescent biosynthetic vacuolar cargo through the Golgi. The results indicate that the vacuolar cargo begins to depart when GGAs arrive, well before the final maturation of late Golgi cisternae into secretory vesicles. Thus, the late/TGN stage of Golgi maturation can be divided into an first sub-stage marked by the exit of vacuolar cargoes to PVE compartments, followed by a second sub-stage marked by AP-1-dependent intra-Golgi recycling and by the exit of secretory cargoes to the plasma membrane.

Second, how is material transferred from PVE compartments to the vacuole? Again, the answer was thought to be known, but 4D microscopy offers a new perspective. By analogy to mammalian cells, it had been assumed that in yeast, early endosomes would mature into PVE compartments that would be consumed by fusing with the vacuole (Balderhaar and Ungermann, 2013; Feyder et al., 2015). Yet maturation of PVE compartments has not been observed—and indeed, if we are correct that yeast cells lack distinct early endosomes, then maturation of yeast endosomes is logically precluded (Day et al., 2018). The implication is that PVE compartments are not continually regenerated and must therefore be stable organelles. In support of this concept, our previous live-cell imaging revealed that PVE compartments undergo fusion and fission but otherwise persist indefinitely (Day et al., 2018). Evidence presented here indicates that stable PVE compartments deliver their contents to the vacuole by transient kiss-and-run fusion events.

Results

Addition of a tetrapeptide generates a fluorescent biosynthetic vacuolar cargo

Because no tool was readily available to create a wave of fluorescent vacuolar cargo, we modified a recently developed regulatable fluorescent secretory cargo (Casler and Glick, 2019; Casler et al., 2019). Our secretory cargo consists of the tetrameric red fluorescent protein DsRed-Express2 fused to a dimerizing variant of FKBP, with a cleavable N-terminal signal sequence to direct cotranslational translocation into the ER. The signal sequence is followed by a tripeptide ER export signal (Yin et al., 2018) and a signal for *N*-linked glycosylation (***Figure 1B***). This fusion protein forms fluorescent aggregates within the ER lumen, and the aggregates can be dissolved by adding a synthetic ligand of FKBP (SLF) that blocks dimerization of FKBP (***Figure 1A***). Soluble tetramers then exit the ER in a nearly synchronized wave. Efficient dissolution of the aggregates requires a drug-sensitive yeast strain. Thus, all of our experiments with the regulatable cargoes employed yeast strains containing deletions of the transcription factors Pdr1 and Pdr3, which mediate pleiotropic drug resistance (Schüller et al., 2007; Coorey et al., 2015; Barrero et al., 2016; Casler et al., 2019). We found previously that the regulatable secretory cargo persists in cisternae through the early-to-late transition of Golgi maturation, and that a fraction of the cargo molecules are recycled within the Golgi in an AP-1-dependent manner (Casler et al., 2019). The goal was to perform similar experiments with a modified cargo that was targeted to the vacuole.

Our strategy was to augment the fusion protein with a vacuolar targeting signal. An obvious candidate for this signal was the propeptide of the vacuolar hydrolase CPY. Prior studies showed that within the propeptide, the tetrapeptide QRPL is necessary and sufficient to direct CPY from the Golgi to PVE compartments by means of the sorting receptor Vps10 (Johnson et al., 1987; Valls et al., 1987; Valls et al., 1990; Marcusson et al., 1994). We flanked QRPL with glycine/serine spacers by appending at the C-terminus of the fusion protein the peptide GSQRPLGGS (***Figure 1B***). The C-terminus was chosen because insertion of QRPL near the N-terminus of the mature protein prevented robust ER aggregation (data not shown). Addition of the QRPL-containing decapeptide at the C-terminus preserved the formation of aggregates within the lumen of the ER, which was marked by GFP-tagged Erg11 (***Figure 1C***). We noted that some cargo molecules were already present in the vacuole prior to dissolution of the aggregates (arrows in ***Figure 1C***), presumably because signal-dependent ER exit was in kinetic competition with aggregate formation (Casler et al., 2019). This QRPL-containing construct was a candidate for a regulatable fluorescent vacuolar cargo.

To test if the QRPL signal worked as intended, we tested non-aggregating (and therefore non-regulatable) versions of the secretory and vacuolar cargoes. The vacuolar membrane was visualized with Vph1-GFP. Compared to the non-aggregating secretory cargo, which accumulated at low levels in the vacuole (Casler et al., 2019), the non-aggregating vacuolar cargo accumulated at high levels in the vacuole in a Vps10-dependent manner (***Figure 1D,E***). A final control experiment used the regulatable versions of the cargoes once again. At 30 min after addition of SLF, the regulatable secretory cargo was detected in the culture medium whereas the regulatable vacuolar cargo was not (***Figure 1F***). These results confirm that the vacuolar cargo traffics efficiently to the vacuole. For convenience, from now on we will refer to the regulatable fluorescent secretory cargo and the regulatable fluorescent vacuolar cargo as the secretory and vacuolar cargoes, respectively.

136
137 **Traffic of the vacuolar cargo can be visualized**
138 We first measured the overall rate of cargo traffic from the ER to the vacuole. A *VPS10* wild-type
139 strain and a *vps10*Δ mutant strain expressed the vacuolar cargo together with the vacuole marker
140 Vph1-GFP. After SLF was added to initiate cargo transport, the cells were imaged by 4D confocal
141 microscopy for 60 min (***Movie 1*** and ***Figure 2A-C***). With *VPS10* cells, we saw a gradual
142 accumulation of fluorescence in the vacuole. With *vps10*Δ cells, virtually no fluorescence
143 appeared in the vacuole, presumably because the cargo exited the cell in secretory vesicles (see
144 below, ***Figure 6—figure supplement 2***). In typical *VPS10* cells, small amounts of the cargo were
145 detected in the vacuole within 8-15 min after SLF addition, and full delivery to the vacuole required
146 at least 40 min (***Figure 2B,C***). Individual cells showed significant variations in the timing of cargo
147 traffic. About 35% of the cells required more than 15 min—and in some cases, more than 25
148 min—before any cargo appeared in the vacuole (***Figure 2B,D***). On average, the cell population
149 showed a gradual increase in vacuolar fluorescence over a time course of an hour (***Figure 2C***).
150 A potential concern with this analysis is that during the time interval examined, new cargo
151 molecules were being synthesized, and some of those molecules could have become fluorescent
152 and reached the vacuole. We addressed this issue by repeating the experiment after pre-treating
153 the cells with cycloheximide to block protein synthesis. Following SLF addition, untreated and
154 cycloheximide-treated cells showed similar traffic kinetics, with cycloheximide causing only a
155 modest reduction in the amount of cargo accumulating in the vacuole even though cell growth
156 was arrested (***Figure 2—figure supplement 1***). We conclude that to a close approximation, the
157 kinetics observed in the absence of cycloheximide reflect traffic of the vacuolar cargo molecules
158 that were originally in ER-localized aggregates.
159 Why is traffic to the vacuole so slow? For comparison, secretory cargo molecules can
160 travel from the ER to the plasma membrane within 5-10 min, and nearly all of them are secreted
161 within 20 min (Losev et al., 2006; Casler et al., 2019). This effect is seen in the *vps10*Δ cells
162 because in the absence of a sorting receptor, the vacuolar cargo behaves like a secretory cargo
163 (***Figure 2A***). To understand the slow kinetics of cargo delivery to the vacuole, we set out to track
164 the different steps of this pathway by fluorescence microscopy.
165
166 **The vacuolar cargo transits rapidly through the Golgi and accumulates in PVE**
167 **compartments**
168 Early work suggested that the rate-limiting step in biosynthetic cargo transport to the vacuole is
169 exit from PVE compartments (Vida et al., 1993). To test this idea, we used three-color 4D confocal
170 movies to visualize the red fluorescent cargo together with the early Golgi marker GFP-Vrg4 and
171 the late Golgi marker Sec7-HaloTag, or together with the PVE marker Vps8-GFP and the vacuole
172 marker Vph1-HaloTag (Losev et al., 2006; Arlt et al., 2015; Day et al., 2018). In this and
173 subsequent experiments, HaloTag was conjugated to the far-red dye JF_{646} (Grimm et al., 2015).
174 After the cargo aggregates were solubilized with SLF, a strain expressing the vacuolar cargo plus
175 the Golgi markers was imaged every 30 s for 29.5 min, and a strain expressing the vacuolar cargo
176 plus the PVE and vacuole markers was imaged every 60 s for 60 min. The results showed cargo
177 accumulation within Golgi compartments 1-5 min after SLF addition, followed by nearly complete
178 transfer of the cargo to PVE compartments by 10 min (***Movie 2*** and ***Movie 3*** and ***Figure 3A-D***).
179 Subsequently, the cargo gradually exited the PVE compartments, and then accumulated in the

vacuole as described above. These results confirm that the rate-limiting step in traffic to the vacuole is not movement through the Golgi, but rather transfer of the cargo from PVE compartments to the vacuole.

Interestingly, although most of the early Golgi cisternae contained detectable vacuolar cargo at early time points, only about half of the late Golgi cisternae ever contained detectable vacuolar cargo (***Figure 3C***). By contrast, we previously saw that the fluorescent secretory cargo was present in nearly all of the late Golgi cisternae, where it persisted until the final phase of maturation (Casler et al., 2019). A possible explanation is that the vacuolar cargo departed during the late stage of Golgi maturation, so that as late Golgi cisternae became more mature, they no longer contained fluorescent cargo. To test this hypothesis, we next visualized the dynamics of the vacuolar cargo in maturing Golgi cisternae.

The vacuolar cargo begins to exit the Golgi near the midpoint of cisternal maturation

To determine when the vacuolar cargo departs from maturing cisternae, we performed 4D confocal microscopy of yeast expressing the vacuolar cargo, the early Golgi marker GFP-Vrg4, and the late Golgi marker Sec7-HaloTag. As previously described, we readily detected Golgi maturation events in which GFP-Vrg4-labeled cisternae lost the GFP-Vrg4 signal as they acquired Sec7-HaloTag, which they subsequently lost at the final phase of maturation (Losev et al., 2006; Casler et al., 2019). Intriguingly, the vacuolar cargo signal began to decline near the midpoint of maturation (***Movie 4***, ***Figure 4A,B***, and ***Figure 4—figure supplement 1A-C***). The rate of decline varied between cells, and qualitative observations indicated that the decline was slower in cells expressing very high levels of the vacuolar cargo (data not shown), probably because the sorting machinery was saturated. Therefore, we focused the analysis on cells expressing moderate levels of the vacuolar cargo. The average behavior over 21 maturation events is depicted in ***Figure 4C***.

We predicted that removal of the Vps10 sorting receptor would prevent normal exit of the vacuolar cargo, which would then behave like a secretory cargo. This prediction was tested by tracking the vacuolar cargo during Golgi maturation in a *vps10*Δ mutant. In the absence of Vps10, the vacuolar cargo signal no longer declined during the early-to-late transition (***Movie 5***, ***Figure 4D-F***, and ***Figure 4—figure supplement 1D-F***). Instead, *vps10*Δ cells actually displayed a transient increase in the cargo signal during the early-to-late transition, likely due to AP-1-dependent recycling from older cisternae as previously shown for the fluorescent secretory cargo (Casler et al., 2019). These data indicate that in wild-type cells, the vacuolar cargo begins to exit the Golgi in a Vps10-dependent manner around the time of the early-to-late transition.

GGAs but not AP-1 are required to sort the vacuolar cargo

To characterize how the vacuolar cargo exits the Golgi, we tested the roles of the AP-1 clathrin adaptor and of the GGA clathrin adaptors Gga1 and Gga2. AP-1 was originally proposed to mediate transport of proteins from the TGN to endosomes (reviewed in Hinners and Tooze, 2003), but subsequent work implicated GGAs in TGN-to-endosome traffic in both yeast and mammalian cells (Black and Pelham, 2000; Dell'Angelica et al., 2000; Hirst et al., 2000; Zhdankina et al., 2001). In *S. cerevisiae*, AP-1 localizes exclusively to the late Golgi, and it mediates intra-Golgi recycling of some resident late Golgi proteins and secretory cargoes (Valdivia et al., 2002; Liu et al., 2008; Papanikou et al., 2015; Spang, 2015; Day et al., 2018; Casler and Glick, 2019). It was

224 previously reported that yeast GGAs function upstream of AP-1 and that GGAs display similar
225 kinetics of arrival and departure as the late Golgi reference marker Sec7 (Daboussi et al., 2012).
226 However, a somewhat different conclusion was presented in a more recent study, which reported
227 that GGAs arrived at Golgi cisternae significantly later than Sec7 (Tojima et al., 2019). To clarify
228 the functions of these adaptors in sorting the vacuolar cargo, we combined a kinetic analysis of
229 AP-1 and GGA dynamics with tests of deletion mutants.
230 If a given adaptor is involved in transporting the vacuolar cargo out of the Golgi, then
231 arrival of that adaptor is expected to coincide with initiation of cargo departure. In a kinetic
232 analysis, we first compared Sec7 with the AP-1 subunit Apl2 and with the major GGA isoform
233 Gga2 (Myers and Payne, 2013). Three-color imaging was performed with Apl2-GFP, Gga2-
234 HaloTag, and Sec7-mScarlet. Gga2 consistently showed arrival and departure kinetics nearly
235 identical to those of Sec7, whereas Apl2 consistently arrived ~20-40 s later and departed ~10-15 s
236 later than Gga2 and Sec7 (***Movie 6***, ***Figure 5A,B***, and ***Figure 5—figure supplement 1A-C***).
237 Thus, GGAs arrive at the Golgi at about the same time that the vacuolar cargo begins to depart.
238 Indeed, when the vacuolar cargo was visualized in maturing cisternae together with the early
239 Golgi marker GFP-Vrg4 and with Gga2-HaloTag, the first appearance of Gga2 occurred at about
240 the same time that the vacuolar cargo signal started to decline (***Movie 7***, ***Figure 5C,D***, and ***Figure***
241 ***5—figure supplement 1D***). Interestingly, the cargo signal would sometimes begin to drop slightly
242 before Gga2 was visible at the Golgi. A potential explanation is that when GGAs are first recruited,
243 they are immediately packaged into vesicles that transport vacuolar cargoes from the Golgi, so
244 the pool of Golgi-associated Gga2 initially remains low. Regardless of whether this interpretation
245 is correct, GGA arrival kinetics closely match the departure kinetics of the vacuolar cargo,
246 whereas AP-1 arrival kinetics do not.
247 If a given adaptor is involved in transporting the vacuolar cargo out of the Golgi, then loss
248 of that adaptor should disrupt normal sorting. We generated an *apl4*Δ deletion strain to inactivate
249 AP-1 and a *gga1*Δ *gga2*Δ double deletion strain to inactivate GGAs, and then tracked the vacuolar
250 cargo together with the early Golgi marker GFP-Vrg4 and the late Golgi marker Sec7-HaloTag.
251 In the *apl4*Δ strain, the vacuolar cargo signal began to decline during the early-to-late transition
252 of Golgi maturation in a manner indistinguishable from that seen in wild-type cells (***Movie 8***,
253 ***Figure 6A-C***, and ***Figure 6—figure supplement 1A-C***). Strikingly, in the *gga1*Δ *gga2*Δ strain,
254 the vacuolar cargo persisted during the early-to-late transition (***Movie 9***, ***Figure 6D-F***, and ***Figure***
255 ***6S—figure supplement 1D-F***). In most of the events analyzed for the *gga1*Δ *gga2*Δ strain, the
256 vacuolar cargo could be detected within the cisterna until the Sec7 signal disappeared or even
257 afterwards (***Figure 6D, E*** and ***Figure 6—figure supplement 1D,E***). A caveat is that the *gga1*Δ
258 *gga2*Δ strain displayed somewhat altered Vrg4 and Sec7 maturation kinetics, as indicated by
259 abnormally shallow slopes for the arrival and departure curves of the Golgi markers (***Figure 6F***).
260 Nevertheless, maturation events could be readily identified in the *gga1*Δ *gga2*Δ strain, and the
261 results strongly suggest that GGAs are needed for the vacuolar cargo to exit the Golgi.
262 As a further test of this interpretation, we hypothesized that loss of GGAs would cause the
263 vacuolar cargo to be secreted, as is true for native CPY (Dell'Angelica et al., 2000; Hirst et al.,
264 2000; Zhdankina et al., 2001). This prediction was tested by an immunoblot of media samples
265 collected 30 min after solublizing the vacuolar cargo with SLF in wild-type, *vps10*Δ*, apl4*Δ*,* and
266 *gga1*Δ *gga2*Δ strains. Secreted cargo was consistently observed with the *vps10*Δ and *gga1*Δ
267 *gga2*Δ strains but not with the wild-type or *apl4*Δ strains (***Figure 6—figure supplement 2A***). As

268 another readout for mistargeting of the vacuolar cargo, we compared the total amount of cargo
269 present in the vacuole 60 min after solubilizing the cargo with SLF in wild-type, *vps10*Δ, *apm3*Δ,
270 *apl4*Δ, and *gga1*Δ*gga2*Δ strains. Apm3 serves as an additional control because it is a subunit of
271 the AP-3 adaptor complex, which functions in a parallel pathway that targets certain membrane
272 proteins directly from the Golgi to the vacuole (Odorizzi et al., 1998; Myers and Payne, 2013).
273 The wild-type, *apl4*Δ, and *apm3*Δ strains all showed similar amounts of vacuolar cargo, while the
274 *vps10*Δ and *gga1*Δ *gga2*Δ strains showed very little vacuolar cargo (***Figure 6—figure***
275 ***supplement 2B,C***). The combined results indicate that the vacuolar cargo is sorted to PVE
276 compartments after the early-to-late Golgi transition, with the aid of Vps10 and GGAs but with no
277 apparent contribution from AP-1.
278

279 **Soluble and transmembrane cargoes transit from PVE compartments to the**
280 **vacuole by kiss-and-run events**

281 Based on the observation that PVE compartments are indefinitely long-lived, we have speculated
282 that PVE compartments deliver cargoes to the vacuole via kiss-and-run fusion events that
283 generate transient pores (Day et al., 2018). Such pores would allow the passage of soluble
284 cargoes as well as intraluminal vesicles that carry membrane-bound cargoes (Henne et al., 2011).
285 This type of partial fusion mechanism could explain why the movement of cargoes from PVE
286 compartments to the vacuole is relatively slow.
287 To test this concept, we developed an assay in which a pool of labeled cargo molecules
288 in a PVE compartment can be tracked during passage to the vacuole. This approach had two
289 technical hurdles: (1) prior to imaging, a fraction of the fluorescent cargo molecules are in the
290 vacuole or other non-PVE compartments, and (2) a typical cell contains several PVE
291 compartments that can undergo fusion and fission (Day et al., 2018), making it difficult to follow
292 individual organelles. The problem with background fluorescence was addressed by
293 photobleaching cargo molecules outside of the PVE compartments. The bleached region
294 comprised the interior of the vacuole plus the portion of the cell outside the vacuole, leaving a ring
295 of non-bleached fluorescence that included the vacuole-associated PVE compartments. The
296 problem of tracking multiple PVE compartments was addressed by focusing on cells that
297 happened to contain just one or two PVE compartments.
298 Traffic of the biosynthetic vacuolar cargo from PVE compartments to the vacuole was
299 visualized by generating a yeast strain expressing the vacuolar cargo together with the PVE
300 marker Vps8-GFP and the vacuole marker Vph1-HaloTag. We and others showed previously that
301 Vps8 is a suitable marker for PVE compartments, and has dynamic behavior similar to that of
302 other PVE markers (Arlt et al., 2015; Day et al., 2018). At 10-15 min after SLF addition, the
303 majority of the cargo molecules had passed through the Golgi and accumulated in PVE
304 compartments (see ***Figure 3C*** above). 4D confocal imaging was then performed after
305 photobleaching the signal outside the PVE compartments. As previously documented (Day et al.,
306 2018), the Vps8-GFP-labeled PVE compartments persisted throughout the imaging period.
307 Meanwhile, cargo fluorescence moved from PVE compartments to the vacuole. Most often, the
308 fluorescence in a PVE compartment gradually declined, and this decrease was matched by a
309 gradual increase of fluorescence in the vacuole (***Movie 10*** and ***Figure 7A,B***). Occasionally, a
310 discrete event rapidly transferred a substantial fraction of the cargo fluorescence to the vacuole
311 (***Movie 11*** and ***Figure 7C,D***). Although the Vps8-GFP signal varied, and sometimes dropped after

312 a discrete event, the punctate PVE compartments marked with Vps8-GFP were never seen to
313 disappear. Our interpretation is that the vacuolar cargo moves from long-lived PVE compartments
314 to the vacuole by a series of kiss-and-run events that are frequently small and sometimes large.
315 We wondered whether such kiss-and-run events could also deliver transmembrane
316 cargoes that are encapsulated in intraluminal vesicles within PVE compartments (Henne et al.,
317 2011). This experiment employed the methionine permease Mup1 as a model transmembrane
318 cargo (Menant et al., 2006). In the absence of methionine in the culture medium, Mup1 resides in
319 the plasma membrane, and upon addition of methionine, Mup1 is ubiquitinated, internalized, and
320 sent to the vacuole for degradation (Lin et al., 2008). We generated a strain expressing Mup1-
321 mScarlet, together with Vps8-GFP to label PVE compartments and Vph1-HaloTag to label the
322 vacuole. Methionine was added for 10-15 min to redistribute Mup1 to PVE compartments, and
323 then cells were subjected to 4D confocal imaging after photobleaching the signal outside the PVE
324 compartments, as described above for the soluble vacuolar cargo. Once again, kiss-and-run
325 events were readily observed. The Mup1 cargo moved from PVE compartments to the vacuole,
326 sometimes gradually and sometimes in bursts (***Movie 12*** and ***Figure 8A,B***). Occasionally, a
327 dramatic event results in transfer of virtually all of the cargo in a single burst (***Movie 13*** and ***Figure***
328 ***8C,D***). We never observed complete loss of Vps8 as would be expected for a full fusion event,
329 although a subset of the larger large kiss-and-run events led to significant reduction in the Vps8
330 signal (***Movie 14*** and ***Figure 8—figure supplement 1***). The results obtained with Mup1 match
331 those obtained with the biosynthetic vacuolar cargo, and they favor a kiss-and-run mechanism.

Discussion

332 Live-cell fluorescence microscopy complements other methods by providing unique insights into
333 membrane traffic (Lippincott-Schwartz et al., 2000). Recently, we engineered a regulatable
334 fluorescent secretory cargo that can be visualized during yeast Golgi maturation (Casler and
335 Glick, 2019; Casler et al., 2019). This secretory cargo is present in Golgi cisternae throughout the
336 maturation process, and a substantial portion of the cargo molecules recycle from older to
337 younger cisternae by an AP-1-dependent pathway (Casler et al., 2019). As an extension of that
338 work, we have now generated a regulatable fluorescent vacuolar cargo that can be tracked in
339 yeast cells. This vacuolar cargo follows the well characterized pathway by which CPY travels from
340 the Golgi to PVE compartments, with the aid of Vps10 and the GGAs, before reaching the vacuole
341 (Bowers and Stevens, 2005; Hecht et al., 2014).

342 The convenience of working with an artificial vacuolar cargo is accompanied by some
343 caveats. Compared to CPY, which is monomeric (Endrizzi et al., 1994), our vacuolar cargo is a
344 tetramer and thus contains four copies of the Vps10 recognition signal. Moreover, Vps10 has a
345 quality control domain that recognizes the fluorescent protein component of the cargo (Fitzgerald
346 and Glick, 2014; Casler et al., 2019), so there are multiple points of interaction between Vps10
347 and the artificial vacuolar cargo. A consequence is that our vacuolar cargo might dissociate from
348 Vps10 more slowly than CPY dissociates, leading to slower PVE-to-vacuole delivery. However,
349 this possible effect on traffic kinetics should not compromise interpretations about the pathway of
350 cargo transport from the Golgi to the vacuole.

351 Using the vacuolar cargo, we asked a basic question: at what point during cisternal
352 maturation does the vacuolar cargo depart from the Golgi? Unlike the regulatable fluorescent
353 secretory cargo, which persists in Golgi cisternae until they are terminally mature (Casler et al.,
354 2019), the vacuolar cargo begins to depart during the early-to-late Golgi transition. Departure of
355 the vacuolar cargo begins at about the same time that the GGAs arrive at the Golgi, and well
356 before AP-1 arrives. Moreover, departure of the vacuolar cargo is abolished by deleting the GGAs
357 but is unaffected by deleting AP-1. These results fit with previously published data indicating that
358 the CPY pathway from the Golgi to the PVE involves GGAs but not AP-1 (Dell'Angelica et al.,
359 2000; Hirst et al., 2000; Hirst et al., 2001; Zhdankina et al., 2001). The new insight is that departure
360 of the vacuolar cargo from the Golgi begins relatively early, about half way through the time course
361 of cisternal maturation (***Figure 9A***).

362 Superficially, these results are at odds with the established view that various types of
363 biosynthetic cargoes travel through the entire Golgi until being packaged into distinct carriers at
364 the TGN (Griffiths and Simons, 1986; De Matteis and Luini, 2008). While there is evidence that
365 biosynthetic cargoes begin to segregate early in the mammalian Golgi, all of those cargoes are
366 thought to reach the terminal TGN compartment (Chen et al., 2017). But we suggest that there is
367 actually no discrepancy between the yeast and mammalian data. In a typical cultured mammalian
368 cell, the early Golgi consists of about six cisternae whereas the clathrin-labeled TGN is a single
369 cisterna (Ladinsky et al., 1999; Mogelsvang et al., 2004). In yeast, the ratio is different because
370 the clathrin-labeled late Golgi/TGN stage occupies about half of the maturation time course
371 (***Figure 9B***). In both cell types, GGA-dependent transport occurs during the TGN stage, but the
372 yeast system has allowed us to define a first TGN sub-stage marked by GGA activity followed by
373 a second TGN sub-stage marked by AP-1 activity (***Figure 9A***). Mammalian TGN structures

374 probably undergo a similar kinetic evolution because the interactions of clathrin adaptors at the
375 mammalian TGN resemble those at the yeast TGN (Daboussi et al., 2017). A proposed unified
376 view is that during traffic to either yeast PVE compartments or mammalian late endosomes, GGA-
377 dependent export from the TGN begins prior to secretory vesicle formation and AP-1-dependent
378 intra-Golgi recycling (Pantazopoulou and Glick, 2019).

379 After the vacuolar cargo reaches PVE compartments, how does it move to the vacuole?
380 Previously, based on evidence that PVE compartments are long-lived organelles that rarely if ever
381 fuse completely with the vacuole, we proposed that transfer of material from PVE compartments
382 to the vacuole might involve kiss-and-run fusion events (Day et al., 2018). This model seemed
383 plausible because mammalian cells can employ kiss-and-run fusion to deliver material from late
384 endosomes to lysosomes (Bright et al., 2005; Bright et al., 2016). Here, we have tested the kiss-
385 and-run hypothesis by fluorescence microscopy. A photobleaching protocol generated a cell in
386 which we could image a single PVE compartment containing fluorescent vacuolar cargo
387 molecules, and the fate of that cohort of molecules was tracked over time. We observed gradual
388 transfer of the cargo molecules to the vacuole over tens of minutes, punctuated by occasional
389 larger events involving sudden transfer of a significant fraction of the cargo molecules. The PVE
390 compartments persisted after cargo transfer. Qualitatively similar results were seen when PVE
391 compartments were loaded with fluorescently tagged molecules of the methionine permease
392 Mup1, which is internalized for degradation after methionine is added to the medium (Menant et
393 al., 2006). Mup1 is packaged into intraluminal vesicles within PVE compartments (Lin et al., 2008),
394 implying that the kiss-and-run fusion pores are large enough to transfer intraluminal vesicles. The
395 observed fluctuations in the rate of cargo delivery from PVE compartments to the vacuole suggest
396 that kiss-and-run fusion events vary in size and duration.

397 Our inference about the kiss-and-run mechanism is based on fluorescence microscopy
398 and will benefit from validation by other methods. Notably, an electron tomographic reconstruction
399 carried out by the Odorizzi group (McNatt et al., 2007), reprinted here as ***Figure 8—figure***
400 ***supplement 2***, shows tubular membrane connections between PVE compartments and the
401 vacuole. Our results suggest that such tubular connections should be common, so their
402 prevalence could be quantified in future morphological studies. A separate electron tomographic
403 analysis highlighted a possible complication—PVE compartments were sometimes observed to
404 form clusters (Adell et al., 2017). If a single PVE compartment in a cluster fused completely with
405 the vacuole, the fluorescence from the remaining PVE compartments in the cluster would persist,
406 yielding a false impression of kiss-and-run fusion. Although we cannot rule out this scenario, it
407 seems unlikely, because some PVE compartments are presumably solitary and yet we have
408 never seen one disappear by fusing completely with the vacuole.

409 Cargo transfer from PVE compartments to the vacuole is slow relative to other membrane
410 traffic steps in budding yeast. Historically, kinetics of traffic to the vacuole have been measured
411 by pulse-chase experiments that rely on the maturation of CPY by vacuolar proteases (Stevens
412 et al., 1982; Vida et al., 1993), but those results may be misleading because kiss-and-run fusion
413 could result in some vacuolar proteases being present and active in PVE compartments (Bright
414 et al., 2016). As judged by fluorescence microscopy, PVE-to-vacuole transfer often requires 30
415 min or more to reach completion. By comparison, transit from the ER to the PVE along the
416 biosynthetic pathway and from the plasma membrane to the PVE along the endocytic pathway
417 are largely complete within 10 min (Losev et al., 2006; Day et al., 2018; Casler et al., 2019). A

418 possible reason for PVE-to-vacuole traffic being rate-limiting is that the cell has the option to
419 “change its mind” by recycling membrane proteins from the PVE instead of degrading them (Ma
420 and Burd, 2020). Meanwhile, the AP-3-driven pathway of direct Golgi-to-vacuole traffic offers an
421 alternative for rapid delivery of membrane proteins to the vacuole (Odorizzi et al., 1998).

Acknowledgments

Thanks for assistance with fluorescence microscopy to Christine Labno and Vytas Bindokas at the Integrated Microscopy Core Facility. Additional thanks to Matt West and Greg Odorizzi for alerting us to their relevant electron tomography data and for providing an image to be reproduced here, to Luke Lavis for providing the JF_{646} dye, and to the Glick laboratory for helpful feedback.

This work was supported by National Institutes of Health (NIH) grant R01 GM104010. J.C. Casler was supported by NIH training grant T32 GM007183. The Integrated Microscopy Core Facility is supported by the NIH-funded Cancer Center Support Grant P30 CA014599.

Competing Interests

The authors declare no competing interests.

Materials and Methods

431 **Yeast growth and strain construction**

432 The parental haploid strain was JK9-3da (*leu2-3,112 ura3-52 rme1 trp1 his4*) (Kunz et al., 1993).
433 Yeast were grown with shaking in baffled flasks at 23°C in nonfluorescent minimal glucose
434 dropout medium (NSD) (Bevis et al., 2002) or in rich glucose medium (YPD) supplemented with
435 adenine and uracil.

436 Deletion of the *PDR1*, *PDR3*, and *GGA1* genes was accomplished by replacement with a
437 G418, nourseothricin, or hygromycin resistance cassette from pFA6a-kanMX6, pAG25, or
438 pAG32, respectively (Wach et al., 1994; Goldstein and McCusker, 1999). Deletion of *VPS10*,
439 *APM3*, and *APL4* was accomplished by using overlap extension PCR to generate a hygromycin
440 resistance cassette, amplified from pAG32, flanked by 500 bp upstream and downstream of the
441 gene. Deletion of *GGA2* was accomplished in the same manner, except that the *LEU2* gene from
442 *K. lactis* was amplified from pUG73. The primers used for these procedures are listed in Table 1.

443 Yeast proteins were tagged by gene replacement using the pop-in/pop-out method to
444 maintain endogenous expression levels (Rothstein, 1991; Rossanese et al., 1999). Secretory and
445 vacuolar cargo proteins were expressed using a *TRP1* integrating vector with the strong
446 constitutive *TPI1* promoter and the *CYC1* terminator (Fitzgerald and Glick, 2014). To ensure
447 consistent expression levels, each strain was verified to have a single copy of the integrated
448 plasmid by PCR with the primers listed in Table 1. All plasmids used in this study are documented
449 in the online supplemental material ZIP file, which contains annotated map/sequence files that
450 can be opened with SnapGene Viewer (Insightful Science; https://www.snapgene.com/snapgene-
451 viewer/). [Note to reviewers: this supplemental material will be included in the final submission.]
452 Newly generated plasmids have been submitted to Addgene.
453

454 **Fluorescence microscopy and photobleaching**

455 For live-cell fluorescence imaging, yeast strains were grown in NSD (pH ~5.5) at 23°C. Where
456 indicated, SLF was diluted from a 100 mM stock solution in ethanol (Cayman Chemical;
457 10007974) to a final concentration of 100 µM, and cycloheximide was added from a 100 mg/mL
458 stock solution in DMSO. Cells were attached to a concanavalin A-coated coverglass-bottom dish
459 containing NSD (Losev et al., 2006) for imaging on a Leica SP8 or Leica SP5 confocal microscope
460 equipped with a 1.4 NA/63x oil objective, using a pixel size of 60-80 nm, a Z-step interval of 0.25-
461 0.30 µm, and 20-30 optical sections. The intervals between Z-stacks were based on the needs of
462 the individual experiments.

463 Static images and 4D movies were processed as follows. Static images were converted
464 to 16-bit and average projected (Hammond and Glick, 2000), then range-adjusted to the minimum
465 and maximum pixel values with ImageJ (Schneider et al., 2012). Movies were deconvolved with
466 Huygens Essential (Scientific Volume Imaging) using the classic maximum likelihood estimation
467 algorithm (Day et al., 2017). Movies were converted to hyperstacks and average projected, then
468 range-adjusted to maximize contrast in ImageJ. Custom ImageJ plugins were used to generate
469 montages of time series, select individual structures and remove extraneous structures, convert
470 edited montages to hyperstacks, and measure fluorescence intensities (Johnson and Glick,
471 2019). Each kinetic trace of a fluorescent Golgi marker was normalized to the average of the three

472 highest values measured, a method that provided better results than relying on the single highest
473 signal from a noisy data set.
474 For photobleaching prior to 4D imaging, a region of interest was drawn to include all
475 fluorescent structures within the cell except for the PVE compartments. The regulatable vacuolar
476 cargo and Mup1-mScarlet were bleached by maximum-intensity illumination with a 561-nm laser
477 for 40 s or 5 s, respectively. These bleaching durations were chosen by determining the minimal
478 times needed to bleach the fluorescence signals completely.
479
480 **HaloTag labeling**
481 Proteins modified with HaloTag were labeled as previously described (Casler et al., 2019). Briefly,
482 1 µL of a 1-mM stock solution of JF_{646} ligand (Grimm et al., 2015) in DMSO was diluted in 500 µL
483 NSD and then spun at maximum speed in a microcentrifuge to remove precipitate, and the
484 supernatant was mixed with a 500-µL aliquot of cells. Labeling was performed for 30 min with
485 shaking at 23°C. To remove excess dye, cells were filter-washed by pushing 3 mL of fresh media
486 through the filter. Washed cells were resuspended by pipetting on the filter. The resulting cell
487 mixture was diluted to its original density, and the cells were attached to confocal dishes.
488
489 **Immunoblotting of yeast cell lysates and secreted proteins**
490 Immunoblotting was performed as previously described (Casler et al., 2019). A 5-mL yeast culture
491 was grown in YPD overnight with shaking in a baffled flask to an OD_{600} of 0.7-1.0. The cells were
492 collected by a brief spin in a microcentrifuge, washed twice with fresh YPD, and resuspended in
493 the original volume of fresh YPD. Cultures were treated with 100 µM SLF, and 1.6 mL was
494 removed at each time point. The cells were collected by spinning at 2500xg (5000 rpm) for 2 min
495 in a microcentrifuge. The culture medium supernatant was transferred to a fresh microcentrifuge
496 tube on ice, and the cells were washed once with deionized water. Then the cells were
497 resuspended in 100 µl 4% trichloroacetic acid. Glass beads (0.5-mm; BioSpec Products) were
498 added to bring the total volume to ~200 µl, and the sample was vortexed three times for 1 min
499 each separated by 1-min intervals on ice. Finally, 800 µl of PBS was added, the solution was
500 mixed, and 800 µl of the cell lysate was transferred to a fresh microcentrifuge tube. Supernatant
501 protein samples were precipitated with 4% trichloroacetic acid on ice for 20 min. Precipitated
502 proteins were centrifuged at maximum speed in a microcentrifuge for 15 min at 4°C. Finally, each
503 protein pellet was resuspended in 50 µL SDS-PAGE sample buffer.
504 Treatment with endoglycosidase H was performed as described by the manufacturer (New
505 England Biolabs; P0702S). Briefly, Glycoprotein Denaturing Buffer was added to the protein
506 sample, which was boiled for 5–10 min, followed by addition of GlycoBuffer 3 and
507 endoglycosidase H. The reaction was performed at 37°C for at least 1 h.
508 For immunoblotting, 9 µL of each cell lysate and 14 µL of each secreted protein sample
509 were run on a 4–20% Tris-glycine gel (Bio-Rad; 4561094) together with the Precision Plus Protein
510 Dual Color Standards molecular weight marker (Bio-Rad; 1610374). The separated proteins were
511 transferred to a PVDF membrane (Bio-Rad; 1704156) using the Trans-Blot Turbo system (Bio-
512 Rad). The membrane was blocked with 5% nonfat dry milk in TBST (50 mM Tris-HCl at pH 7.6,
513 150 mM NaCl, and 0.05% Tween 20) with shaking at room temperature for 1 h, and then
514 incubated with 1:1000 polyclonal rabbit anti-FKBP12 antibody (Abcam; ab2918) in 5% milk/TBST
515 with shaking overnight at 4°C. After four 5-min washes in TBST, the membrane was incubated

516 with a 1:1000 dilution of goat anti-rabbit secondary antibody conjugated to Alexa Fluor 647
517 (Thermo Fisher Scientific; A21245) for 1 h at room temperature. The membrane was then washed
518 twice with TBST and twice with 50 mM Tris-HCl at pH 7.6, 150 mM NaCl. Analysis was performed
519 with a LI-COR Odyssey CLx imaging system.

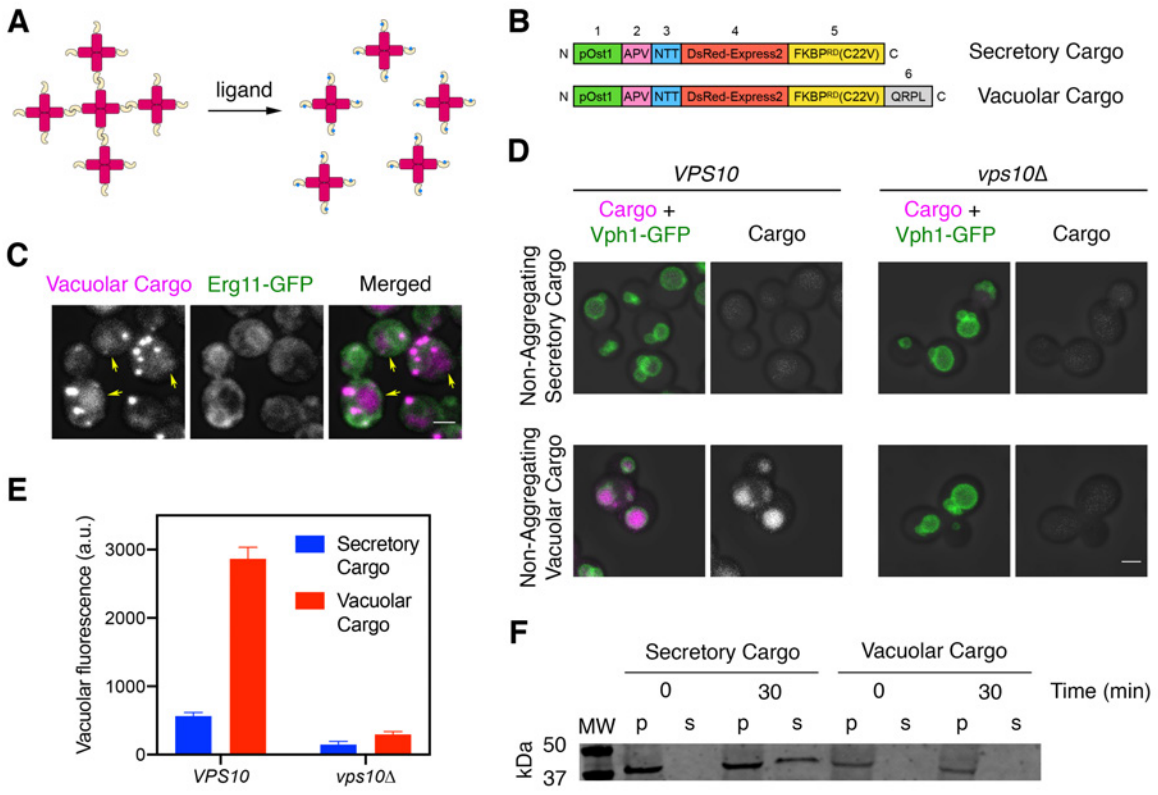

Figure 1. A regulatable vacuolar cargo. (**A**) General strategy for the use of reversibly aggregating fluorescent cargoes. DsRed-Express2 tetramers (red) are linked to a dimerizing FKBP variant (gold), so the tetramers associate to form aggregates. Addition of the FKBP ligand SLF (blue) blocks dimerization, thereby dissolving the aggregates into soluble tetramers that can exit the ER. (**B**) Functional regions of the reversibly aggregating secretory and vacuolar cargoes. The lengths of the regions are not to scale. 1: pOst1 (green) is an ER signal sequence that directs cotranslational translocation. 2: APV (pink) is a tripeptide signal for ER export. 3: NTT (blue) is a tripeptide signal for N-linked glycosylation. 4: DsRed-Express2 (red) is a tetrameric red fluorescent protein. 5: FKBPRD(C22V) (gold) is a reversibly dimerizing variant of FKBP. 6: QRPL (gray) is a tetrapeptide signal for vacuolar targeting. (**C**) Aggregation in the ER of the vacuolar cargo. The ER membrane marker Erg11-GFP (green) confirms that the aggregates (magenta) are in the ER. Yellow arrows point to leaked cargo molecules that have accumulated in the vacuole. Shown are projected confocal Z-stacks. Scale bar, 2 µm. (**D**) Vacuolar targeting by the QRPL tetrapeptide. Non-aggregating variants of the secretory and vacuolar cargoes were expressed in *VPS10* wild-type or *vps10*Δ cells to visualize receptor-dependent targeting to the vacuole, which was marked by the vacuolar membrane marker Vph1-GFP. Significant vacuolar accumulation was seen only in the *VPS10* background when the QRPL signal was present. Shown are projected confocal Z-stacks. Scale bar, 2 µm. (**E**) Quantification of the cargo fluorescence signals in (**D**). The Vph1-GFP signal was used to create a mask for measuring cargo fluorescence in the vacuole. Data are average values from at least 69 cells for each strain. Fluorescence is plotted in arbitrary units (a.u.). Bars represent SEM. (**F**) Immunoblot to measure

541 cell-associated and secreted levels of the secretory and vacuolar cargoes after SLF addition in
542 rich medium. Cells expressing either the secretory or vacuolar cargo were grown to mid-log phase
543 in YPD, washed with fresh YPD, and treated with SLF. At the 0 and 30 min time points, cell-
544 associated pellet ("p") and secreted soluble ("s") fractions were separated by centrifugation.
545 Samples were treated with endglycosidase H to trim *N*-linked glycans, and were analyzed by
546 SDS-PAGE and immunoblotting. Shown is a representative example from four separate
547 experiments. MW, molecular weight markers. The predicted molecular weights for the mature
548 cargoes are ~38-39 kDa. In some samples, the cell-associated vacuolar cargo at the 30-min time
549 point showed evidence of degradation, presumably due to exposure to vacuolar proteases (data
550 not shown).

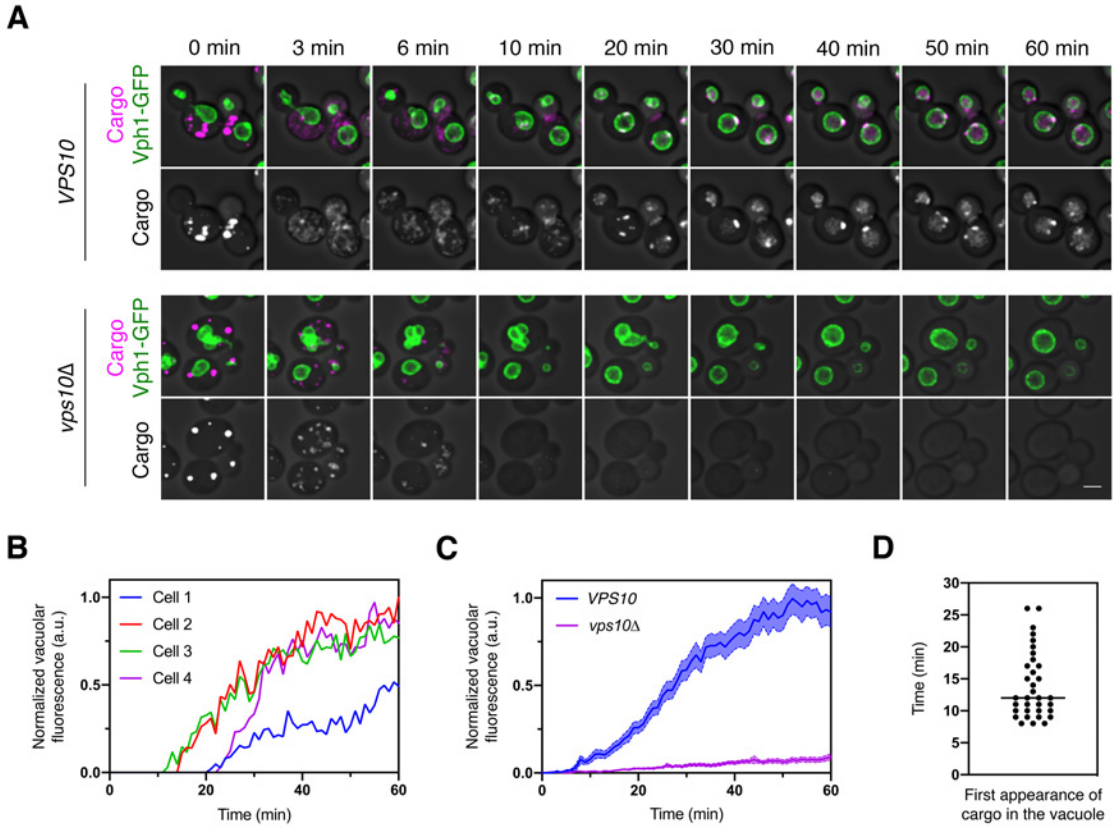

Figure 2. Traffic kinetics of the vacuolar cargo. (**A**) Visualizing cargo traffic. The vacuolar cargo expressed in *VPS10* wild-type or *vps10*Δ strains was imaged by 4D confocal microscopy. Prior to the movie, fluorescence from leaked cargo molecules was bleached by illuminating the vacuole with a 561-nm laser at maximum intensity for 20-30 s. Then SLF was added, and Z-stacks were captured every minute for 60 min. The top panel shows the cargo (magenta) together with the vacuolar membrane marker Vph1-GFP (green), while the bottom panel shows only the cargo. Fluorescence data are superimposed on brightfield images of the cells. Shown are representative frames from ***Movie 1***. Scale bar, 2 μm. (**B**) Quantification of the vacuolar fluorescence from the four *VPS10* cells in (**A**). The Vph1-GFP signal was used to create a mask for measuring cargo fluorescence in the vacuole. Fluorescence is plotted in arbitrary units (a.u.). (**C**) Quantification of the average vacuolar fluorescence in *VPS10* and *vps10*Δ cells after addition of SLF. For each strain, at least 39 cells were analyzed from four movies. Quantification was performed as in (**B**). The shaded borders represent SEM. (**D**) Quantification of the first appearance of cargo fluorescence in the vacuole. Data are from the same set of *VPS10* cells analyzed for (**C**). Appearance in the vacuole was scored as the first time point at which the vacuolar cargo fluorescence reached at least 5% of its final value.

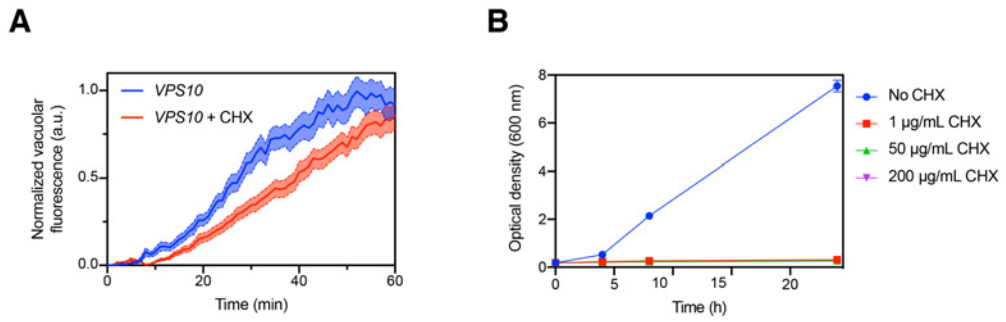

Figure 2—figure supplement 1. Minor effect of cycloheximide treatment on the kinetics of cargo traffic to the vacuole. (**A**) Comparison of traffic kinetics in the absence or presence of cycloheximide (CHX). Data from ***Figure 2C*** were re-plotted with the additional analysis of *VPS10* cells that had been pretreated with 200 µg/mL cycloheximide starting 15 min prior to addition of SLF. (**B**) Control experiment to confirm that cycloheximide potently inhibited protein synthesis. A log-phase culture of *VPS10* cells in YPD medium was diluted to an OD_{600} of 0.2, and growth of the culture was measured over 24 h with or without addition of cycloheximide at the indicated concentrations.

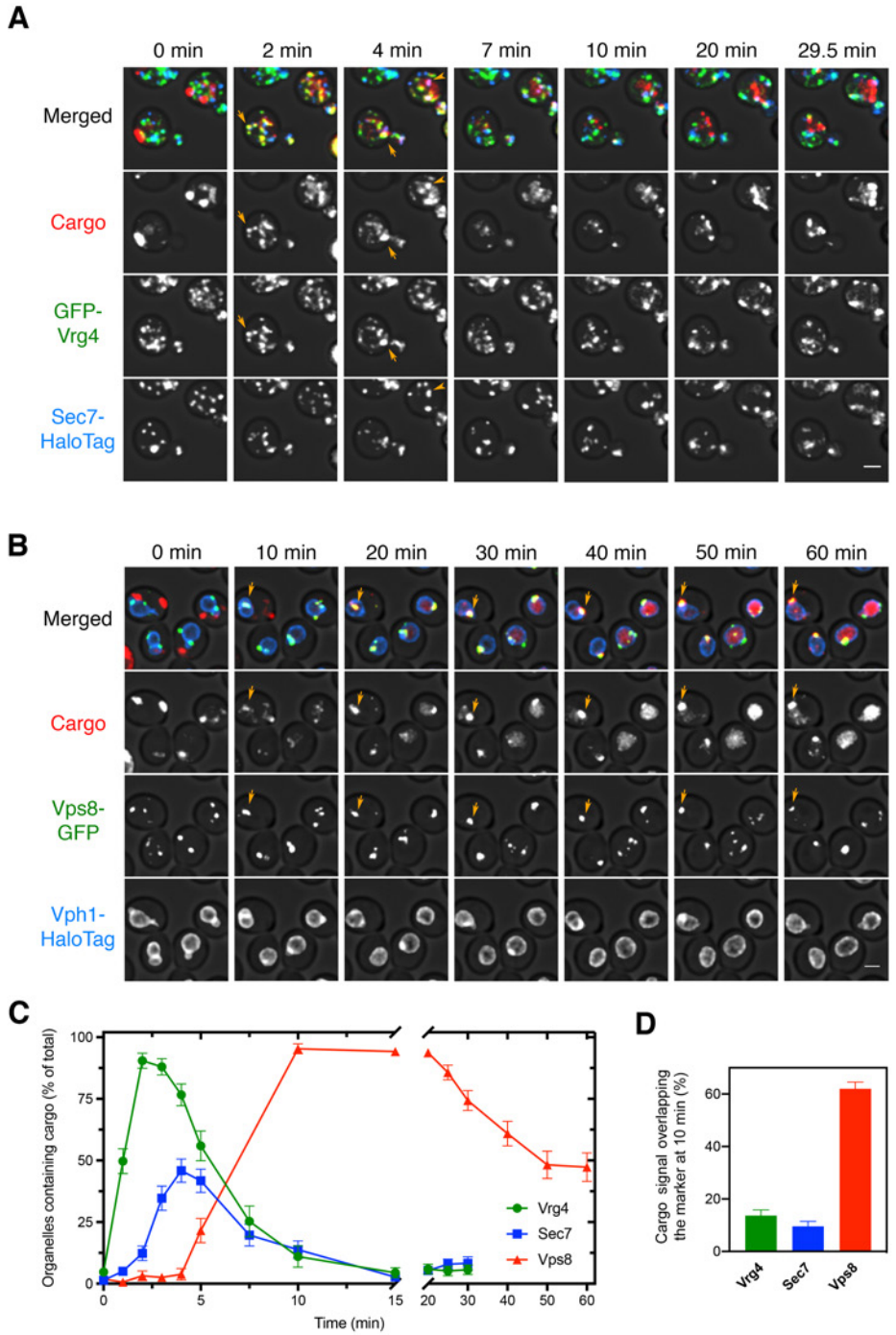

575 **Figure 3.** Sequential appearance of the vacuolar cargo in Golgi and PVE compartments.
576 (**A**) Appearance of the vacuolar cargo in early Golgi compartments labeled with GFP-Vrg4 and
577 in late Golgi compartments labeled with Sec7-HaloTag. Cells were grown to mid-log phase,
578 labeled with JF_{646}, and imaged by 4D confocal microscopy. Prior to beginning the movie,
579 fluorescence from leaked cargo molecules in the vacuole was bleached by illuminating with
580 maximum intensity 561-nm laser power for 20-30 s. SLF was added directly to the dish between

581 the first and second Z-stacks, and then additional Z-stacks were captured every 30 s for 29.5 min.
582 Images are representative time points from ***Movie 2***. The top panel shows the merged images,
583 and the other panels show the individual fluorescence channels for cargo, Vrg4, and Sec7. Scale
584 bar, 2 µm. (**B**) Appearance of the vacuolar cargo in PVE compartments labeled with Vps8-GFP
585 and in the vacuole labeled with Vph1-HaloTag. The procedure was as in (**A**), except that Z-stacks
586 were captured every 1 min for 60 min. Images are representative time points from ***Movie 3***. The
587 top panel shows the merged images, and the other panels show the individual fluorescence
588 channels for cargo, Vps8, and Vph1. Scale bar 2 µm. (**C**) Quantification of the percentage of
589 compartments containing detectable cargo from (**A**) and (**B**). Confocal movies were average
590 projected and manually scored for the presence of cargo in labeled compartments. For each
591 strain, at least 26 cells were analyzed from four movies. The bars represent SEM.
592 (**D**) Quantification of the percentage of the total cargo fluorescence present in early Golgi, late
593 Golgi, and PVE compartments 10 min after SLF addition. The fluorescence for a compartment
594 marker was used to generate a mask to quantify the corresponding cargo fluorescence. Data
595 were taken from at least 26 cells from four movies. The bars represent SEM.

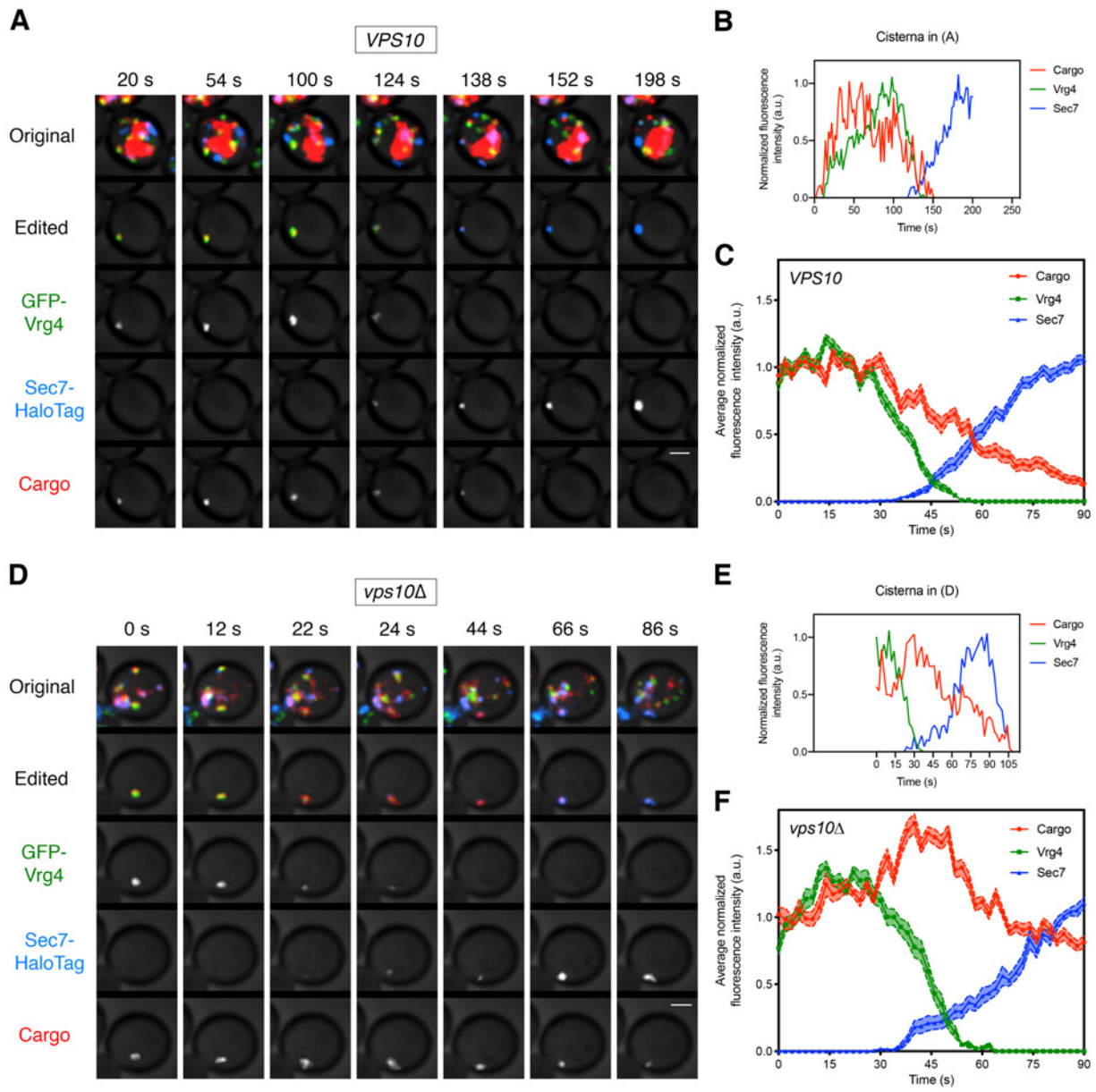

596 **Figure 4.** Visualizing the vacuolar cargo during Golgi maturation. (**A**) Visualizing the vacuolar
597 cargo in a *VPS10* wild-type strain. Cells expressing the vacuolar cargo together with the early
598 Golgi marker GFP-Vrg4 and the late Golgi marker Sec7-HaloTag were grown to mid-log phase,
599 labeled with JF_{646}, and imaged by 4D confocal microscopy. SLF was added 1-3 min before
600 imaging. Shown are average projected Z-stacks at representative time points from ***Movie 4***. The
601 top row shows the complete projection, the second row shows an edited projection that includes
602 only the cisterna being tracked, and the other rows show the individual fluorescence channels
603 from the edited projection. Scale bar, 2 µm. (**B**) Quantification of the fluorescence intensities of
604 the Golgi markers and the vacuolar cargo during a typical maturation event. Depicted are the
605 normalized fluorescence intensities in arbitrary units (a.u.) of the cisterna tracked in (**A**).

606 (**C**) Average cargo signal during the early-to-late Golgi transition. For 21 maturation events from
607 18 movies of cells expressing moderate levels of the vacuolar cargo, fluorescence was quantified
608 over a 90-s window with Z-stacks collected every 2 s. Normalization was performed by defining
609 the maximum value as the average of the first six fluorescence values for the cargo and Vrg4, or
610 of the last six fluorescence values for Sec7. Traces were aligned at the midpoint of the Vrg4-to-
611 Sec7 transition, and the normalized fluorescence signals were averaged. The shaded borders
612 represent SEM. (**D**) Visualizing the vacuolar cargo in a *vps10*Δ strain. The experiment was
613 performed as in (**A**). Shown are average projected Z-stacks at representative time points from
614 ***Movie 5***. (**E**) Quantification of the fluorescence intensities of the Golgi markers and the vacuolar
615 cargo during a typical maturation event in the *vps10*Δ strain. Depicted are the normalized
616 fluorescence intensities in arbitrary units (a.u.) of the cisterna tracked in (**D**). (**F**) Average cargo
617 signal during the early-to-late Golgi transition in a *vps10*Δ strain. The experiment was performed
618 as in (**C**). Data were collected for 12 maturation events from 12 movies of cells expressing
619 moderate levels of the vacuolar cargo.

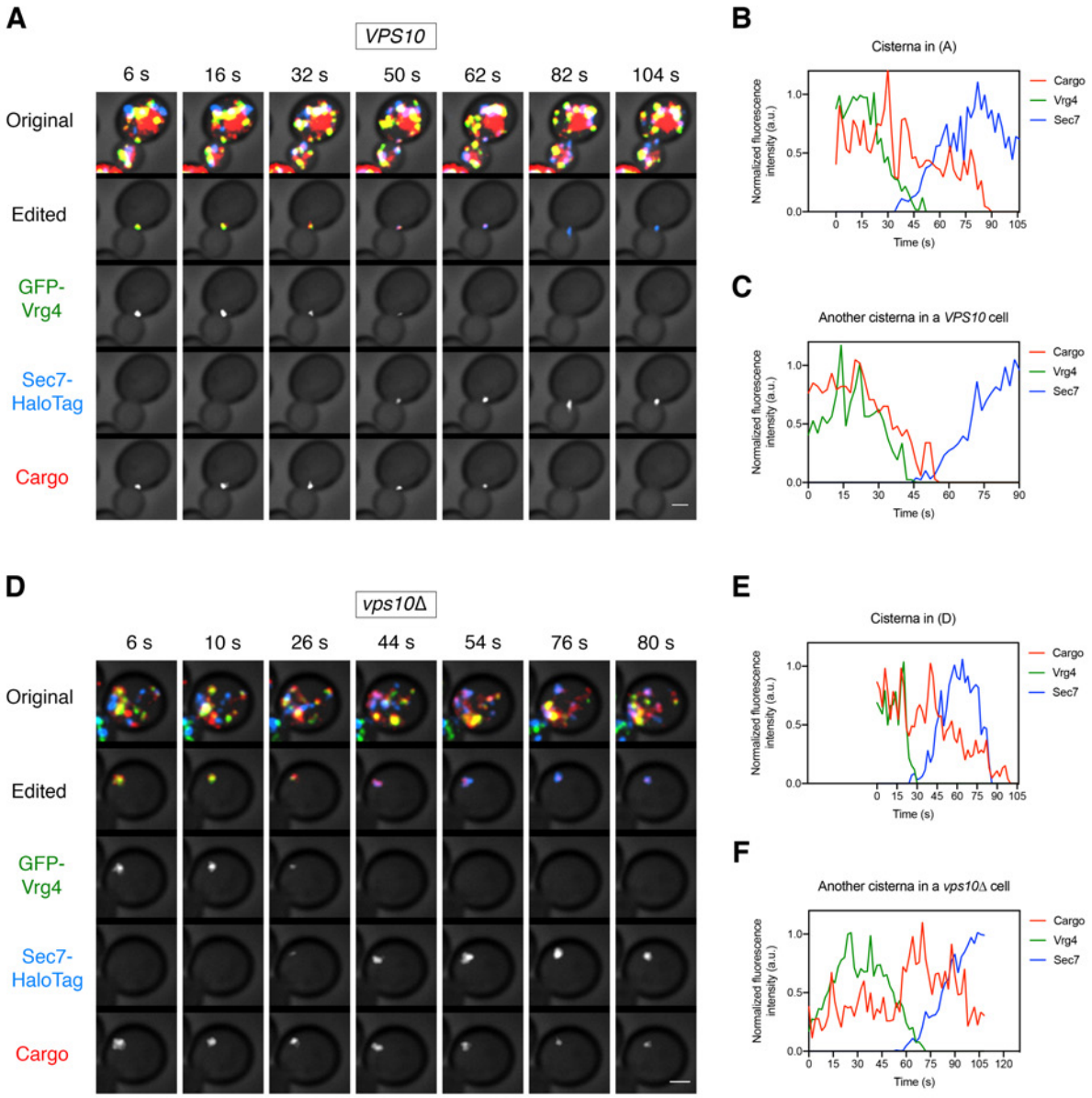

Figure 4—figure supplement 1. Additional examples of vacuolar cargo traffic during Golgi maturation. (**A**) Vacuolar cargo traffic in a *VPS10* wild-type strain. The experiment was performed as in ***Figure 4A***. Shown are average projected Z-stacks at representative time points from an additional movie. The top row shows the complete projection, the second row shows an edited projection that includes only the cisterna being tracked, and the other rows show the individual fluorescence channels from the edited projection. Scale bar, 2 µm. (**B**) Quantification of the fluorescence intensities of the Golgi markers and the vacuolar cargo during maturation of the cisterna tracked in (**A**). The procedure was as in ***Figure 4B***. (**C**) Quantification of a maturation event from an additional movie of a *VPS10* cell. (**D**) – (**F**) Same as (**A**) – (**C**), except that the analysis was performed with a *vps10*Δ strain.

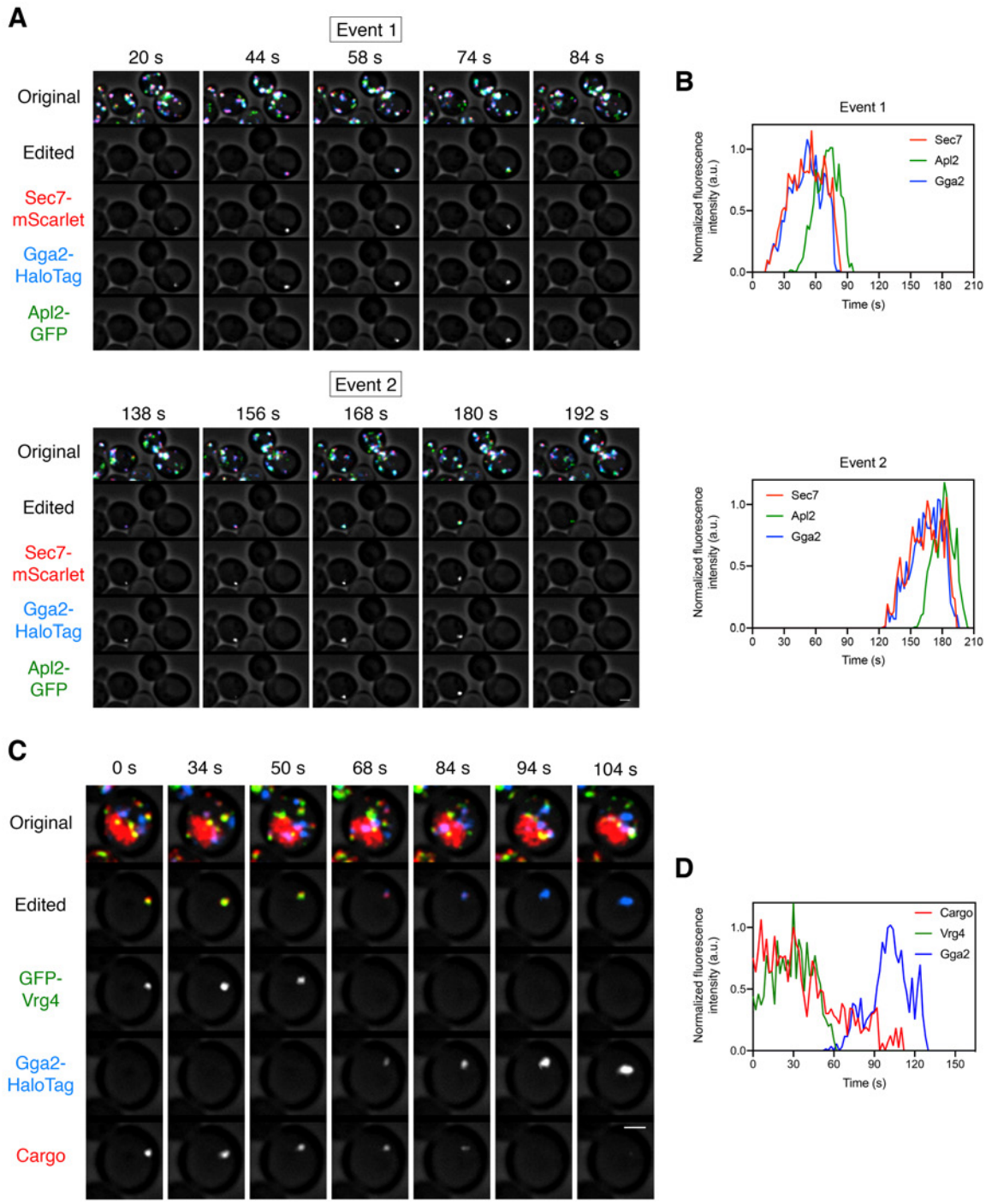

Figure 5. Kinetics of GGA arrival at the Golgi. (**A**) Visualizing the dynamics of the GGA and AP-1 adaptors during cisternal maturation. A strain expressing the GGA protein Gga2-HaloTag, the AP-1 subunit Apl2-GFP, and the late Golgi marker Sec7-mScarlet was grown to mid-log phase, labeled with JF_{646}, and imaged by 4D confocal microscopy. Shown are average projected Z-stacks at representative time points from ***Movie 6***. The top row shows the complete projection, the

635 second row shows an edited projection that includes only the cisterna being tracked, and the other
636 rows show the individual fluorescence channels from the edited projection. Two maturation events
637 are highlighted. Scale bar, 2 μm. (**B**) Quantification of the fluorescence intensities of the late Golgi
638 marker and the clathrin adaptors during typical maturation events. Depicted are the normalized
639 fluorescence intensities in arbitrary units (a.u.) of the two cisternae tracked in (**A**). (**C**) Visualizing
640 Vrg4 and Gga2 together with the vacuolar cargo. The experiment was performed as in ***Figure***
641 ***4A***, except that the Golgi markers were GFP-Vrg4 and Gga2-HaloTag. Shown are average
642 projected Z-stacks at representative time points from ***Movie 7***. The top row shows the complete
643 projection, the second row shows an edited projection that includes only the cisterna being
644 tracked, and the other rows show the individual fluorescence channels from the edited projection.
645 Scale bar, 2 μm. (**D**) Quantification of the fluorescence intensities of the Golgi markers together
646 with the vacuolar cargo during a typical maturation event. Depicted are the normalized
647 fluorescence intensities in arbitrary units (a.u.) of the cisterna tracked in (**C**).

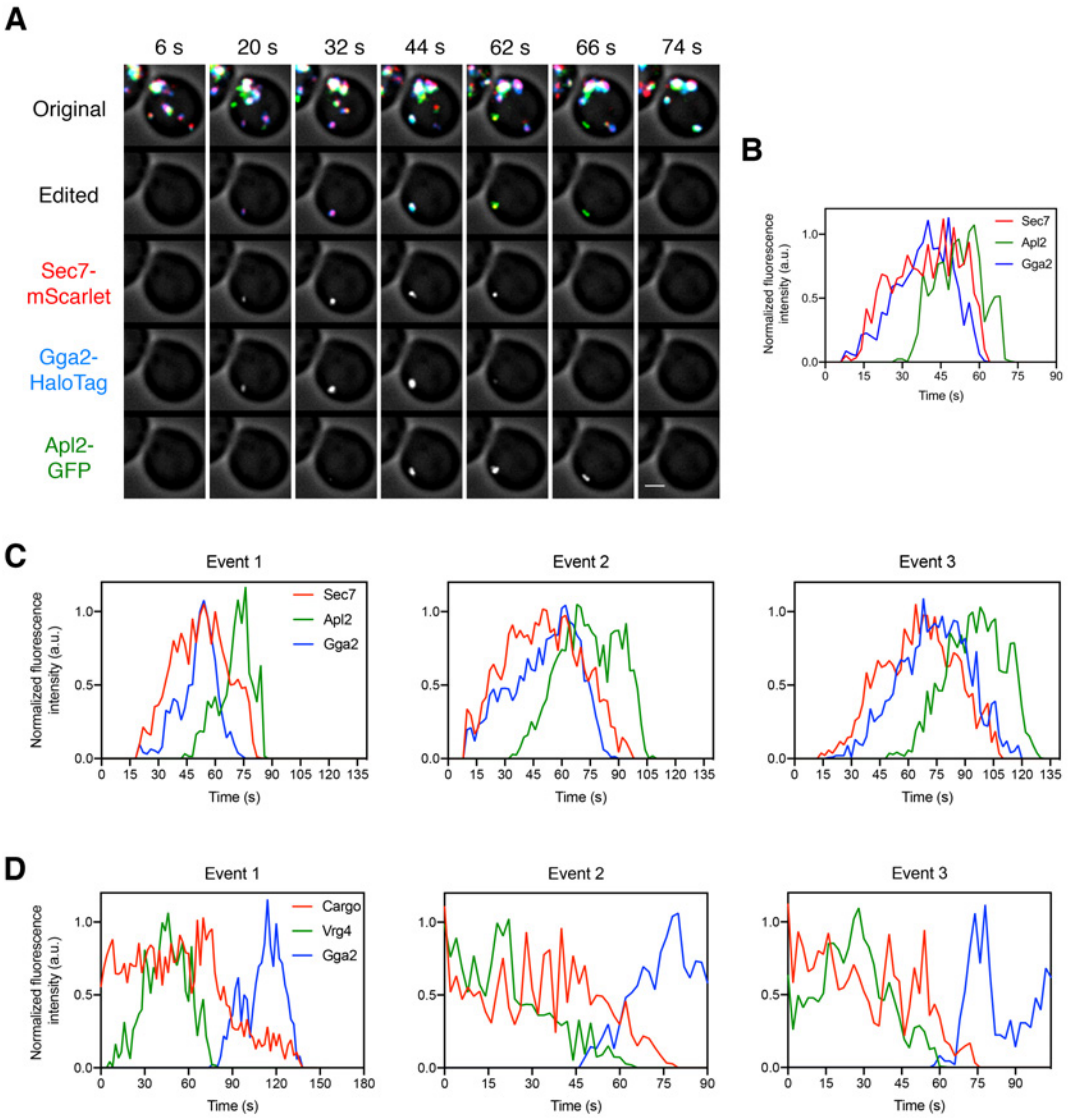

Figure 5—figure supplement 1. Additional examples of clathrin adaptor dynamics and of the relationship between GGA arrival and vacuolar cargo departure. (**A**) Visualizing the dynamics of the GGA and AP-1 adaptors during cisternal maturation. The experiment was performed as in ***Figure 5A***. Shown are average projected Z-stacks at representative time points from an additional movie. The top row shows the complete projection, the second row shows an edited projection that includes only the cisterna being tracked, and the other rows show the individual fluorescence channels from the edited projection. Scale bar, 2 µm. (**B**) Quantification of the fluorescence intensities of the late Golgi marker and the clathrin adaptors during a typical maturation event. Depicted are the normalized fluorescence intensities in arbitrary units (a.u.) of the cisterna tracked in (**A**). (**C**) Quantification of the fluorescence intensities of the late Golgi marker and the clathrin adaptors during three additional maturation events from three additional movies. The analysis was performed as in (**B**). (**D**) Quantification of the fluorescence intensities of the Golgi markers

660 GFP-Vrg4 and Gga2-HaloTag together with the vacuolar cargo during three additional maturation
661 events from three additional movies. The analysis was performed as in ***Figure 5D***.

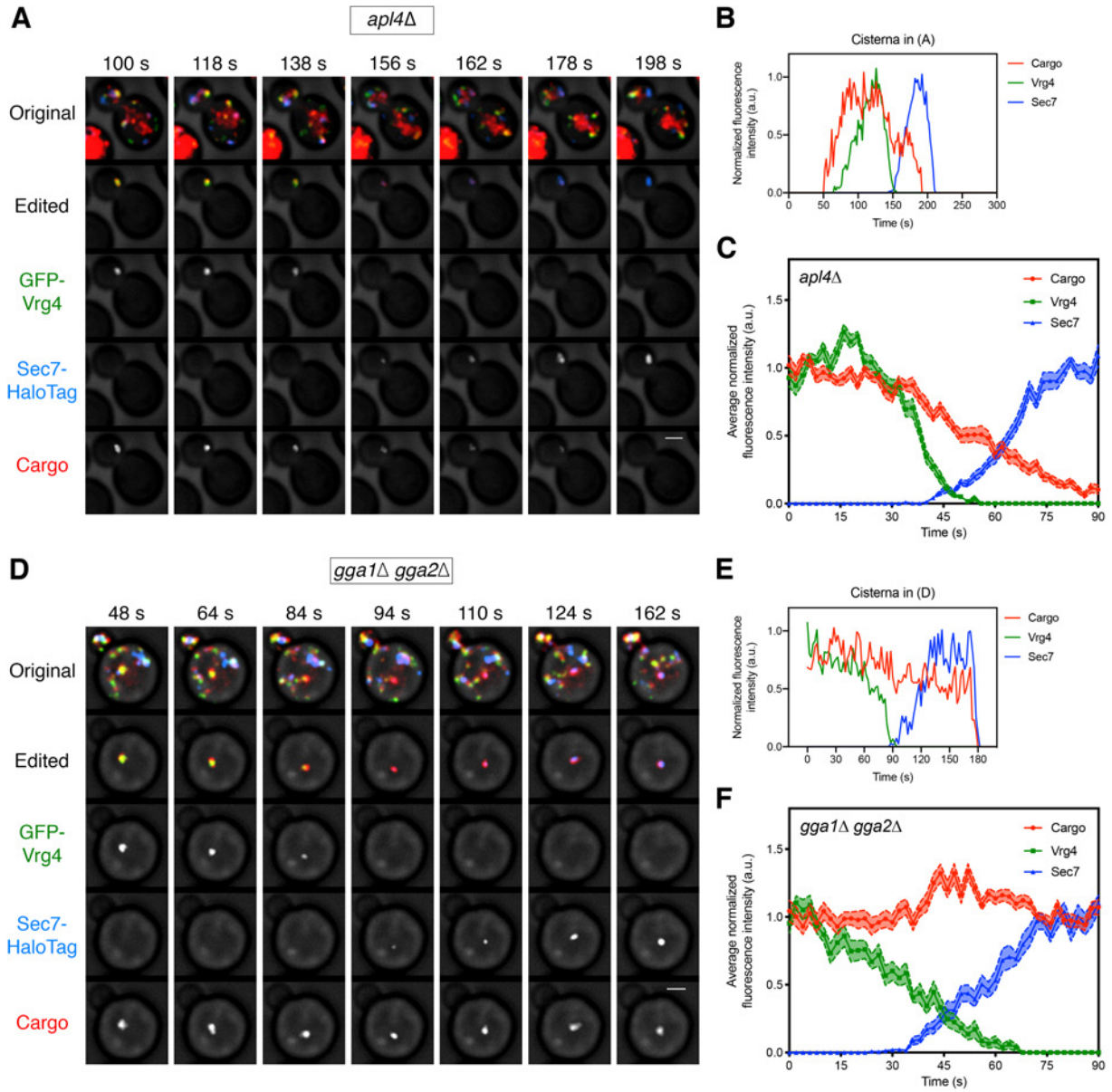

Figure 6. Requirement for the GGAs but not AP-1 during Golgi-to-PVE traffic. (**A**) Visualizing vacuolar cargo traffic during Golgi maturation in a strain lacking AP-1. The experiment was performed as in ***Figure 4A***, except that an *apl4*Δ strain was used. Shown are average projected Z-stacks at representative time points from ***Movie 8***. The top row shows the complete projection, the second row shows an edited projection that includes only the cisterna being tracked, and the other rows show the individual fluorescence channels from the edited projection. Scale bar, 2 µm. (**B**) Quantification of the fluorescence intensities of the Golgi markers and the vacuolar cargo during a typical maturation event in the *apl4*Δ strain. Depicted are the normalized fluorescence intensities in arbitrary units (a.u.) of the cisterna tracked in (**A**). (**C**) Average cargo signal during the early-to-late Golgi transition in the *apl4*Δ strain. The analysis was performed as in ***Figure 4C***, based on 17 maturation events from 13 movies of cells expressing moderate levels of the vacuolar

673 cargo. (**D**) – (**F**) Same as (**A**) – (**C**) except with a *gga1*Δ *gga2*Δ strain lacking GGAs. The analysis
674 in (**C**) was based on 15 maturation events from 12 movies of cells expressing moderate levels of
675 the vacuolar cargo. Shown in (**D**) are average projected Z-stacks at representative time points
676 from ***Movie 9***.

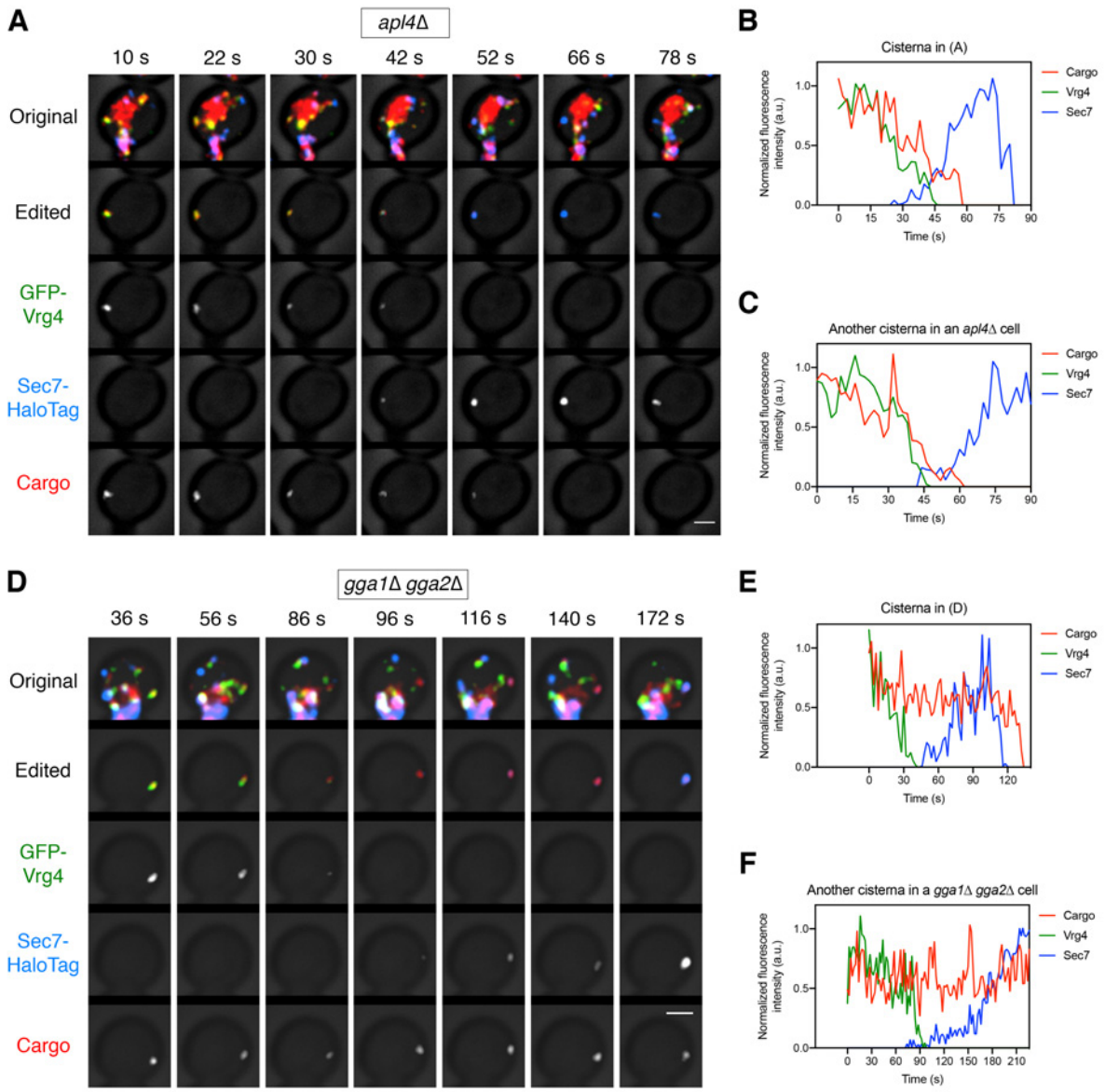

677 **Figure 6—figure supplement 1.** Additional examples of cargo dynamics during cisternal
678 maturation in strains lacking AP-1 or the GGAs. (**A**) Visualizing vacuolar cargo traffic during Golgi
679 maturation in a strain lacking AP-1. The experiment was performed with an *apl4*Δ strain as in
680 ***Figure 6A***. Shown are average projected Z-stacks at representative time points from an additional
681 movie. The top row shows the complete projection, the second row shows an edited projection
682 that includes only the cisterna being tracked, and the other rows show the individual fluorescence
683 channels from the edited projection. Scale bar, 2 µm. (**B**) Quantification of the fluorescence
684 intensities of the Golgi markers and the vacuolar cargo during maturation of the cisterna tracked
685 in (**A**). The procedure was as in ***Figure 6B***. (**C**) Quantification of a maturation event from an
686 additional movie of an *apl4*Δ cell. (**D**) – (**F**) Same as (**A**) – (**C**) except with a *gga1*Δ *gga2*Δ strain
687 lacking GGAs.

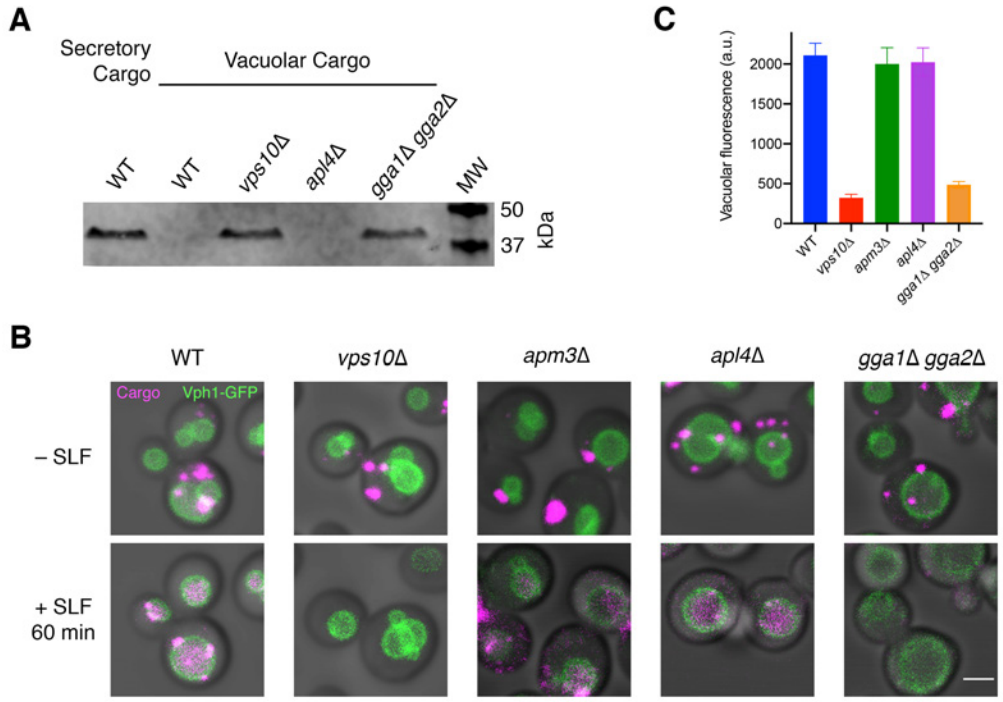

688 **Figure 6s—figure supplement 2.** Secretion of the vacuolar cargo in the absence of Vps10 or
689 the GGAs. (**A**) Immunoblot of secreted cargoes after SLF addition in rich medium. Wild-type (WT)
690 cells expressing the secretory cargo and wild-type, *vps10*Δ*, apl4*Δ*,* and *gga1*Δ *gga2*Δ cells
691 expressing the vacuolar cargo were grown to mid-log phase in YPD, washed with fresh YPD, and
692 treated with SLF. After 30 min, the secreted fractions were isolated by centrifugation, treated with
693 endoglycosidase H to trim *N*-glycans, and analyzed by SDS-PAGE and immunoblotting. Shown
694 is a representative example from four separate experiments. MW, molecular weight markers. The
695 predicted molecular weights for the mature cargoes are ~38-39 kDa. (**B**) Accumulation of the
696 vacuolar cargo in the vacuole after SLF addition in various genetic backgrounds. The vacuolar
697 cargo was expressed in wild-type, *vps10*Δ, *apm3*Δ, *apl4*Δ, and *gga1 gga2*Δ cells that also
698 contained the vacuolar membrane marker Vph1-GFP. The experiment was performed as in
699 ***Figure 2A***. (**C**) Quantification of the amount of cargo reaching the vacuole in (**B**). The Vph1-GFP
700 signal was used to create a mask for measuring cargo fluorescence in the vacuole. Data are
701 average values from at least 37 cells for each strain. Fluorescence is plotted in arbitrary units
702 (a.u.). Bars represent SEM.

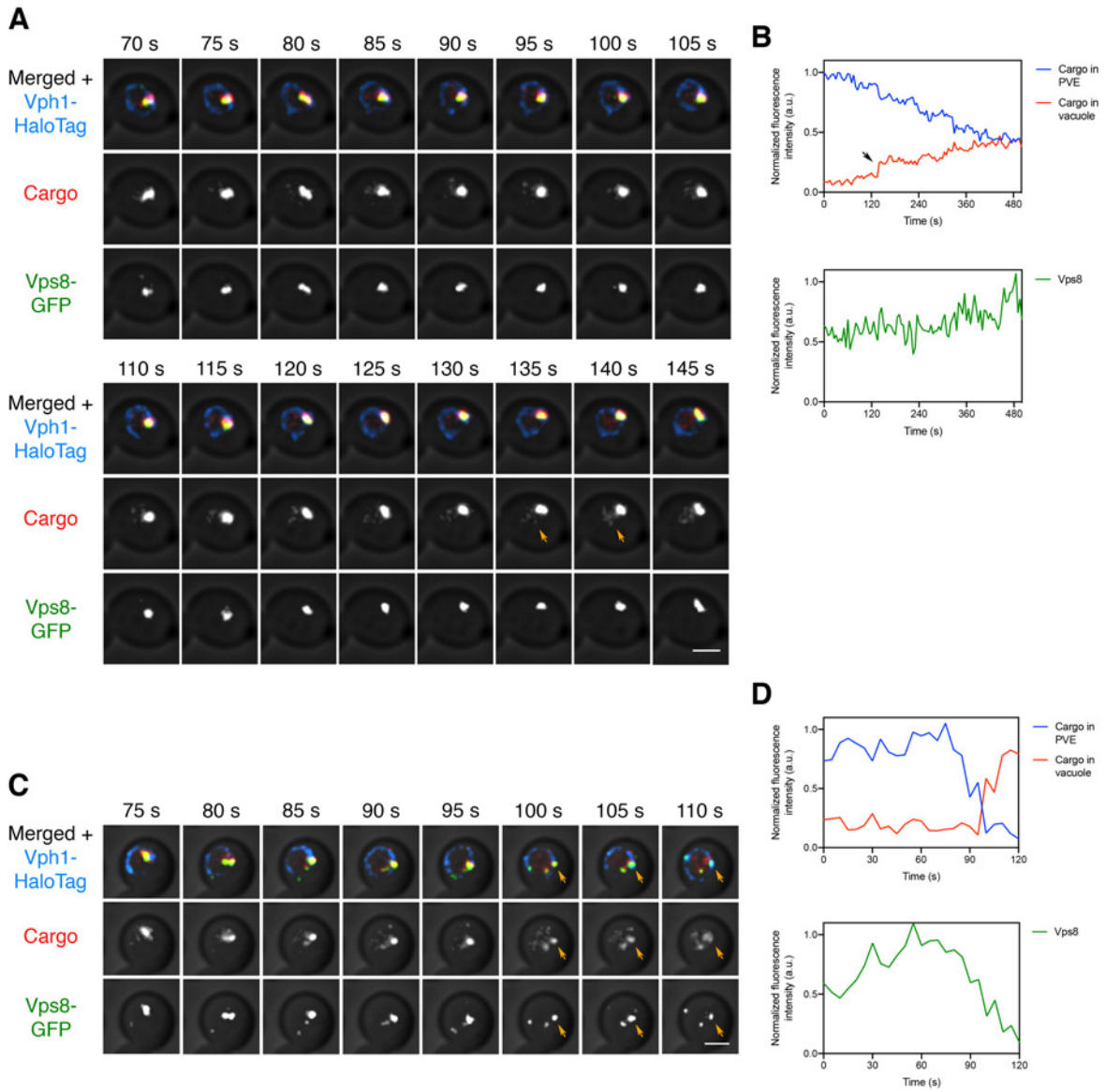

Figure 7. Visualizing transfer of the vacuolar cargo from PVE compartments to the vacuole. (**A**) Gradual movement of the vacuolar cargo from a PVE compartment to the vacuole. A strain expressing the vacuolar membrane marker Vph1-HaloTag, the PVE marker Vps8-GFP, and the vacuolar cargo was grown to mid-log phase, attached to a confocal dish, and treated with SLF for 10-15 min to enable the cargo to reach PVE compartments. Prior to imaging, a region that excluded PVE compartments was photobleached by illumination with maximum intensity 561-nm laser light for 40 s. Shown are frames from ***Movie 10***. The top row shows the complete projection, the middle row shows the cargo fluorescence, and the bottom row shows the Vps8-GFP fluorescence. Orange arrows indicate sudden transfer of a small amount of cargo from the PVE compartment to the vacuole. Scale bar, 2 μm. (**B**) Quantification from (**A**) of the time course of cargo fluorescence in the PVE compartment and the vacuole, and of the Vps8 signal. To quantify the cargo signal at each time point, the Vph1 or Vps8 signal was selected in a 3D volume and

715 then the cargo fluorescence within that volume was measured. Normalized data are plotted in
716 arbitrary units (a.u.). The black arrow points to the same cargo transfer event that is marked by
717 the orange arrows in (**A**). (**C**) Example of sudden transfer of a large amount of cargo from a PVE
718 compartment to the vacuole. The experiment was performed as in (**A**). Shown are frames from
719 ***Movie 11***. Orange arrows indicate an event in which nearly all of the cargo moved from the PVE
720 compartment to the vacuole. (**D**) Quantification of (**C**), performed as in (**B**).

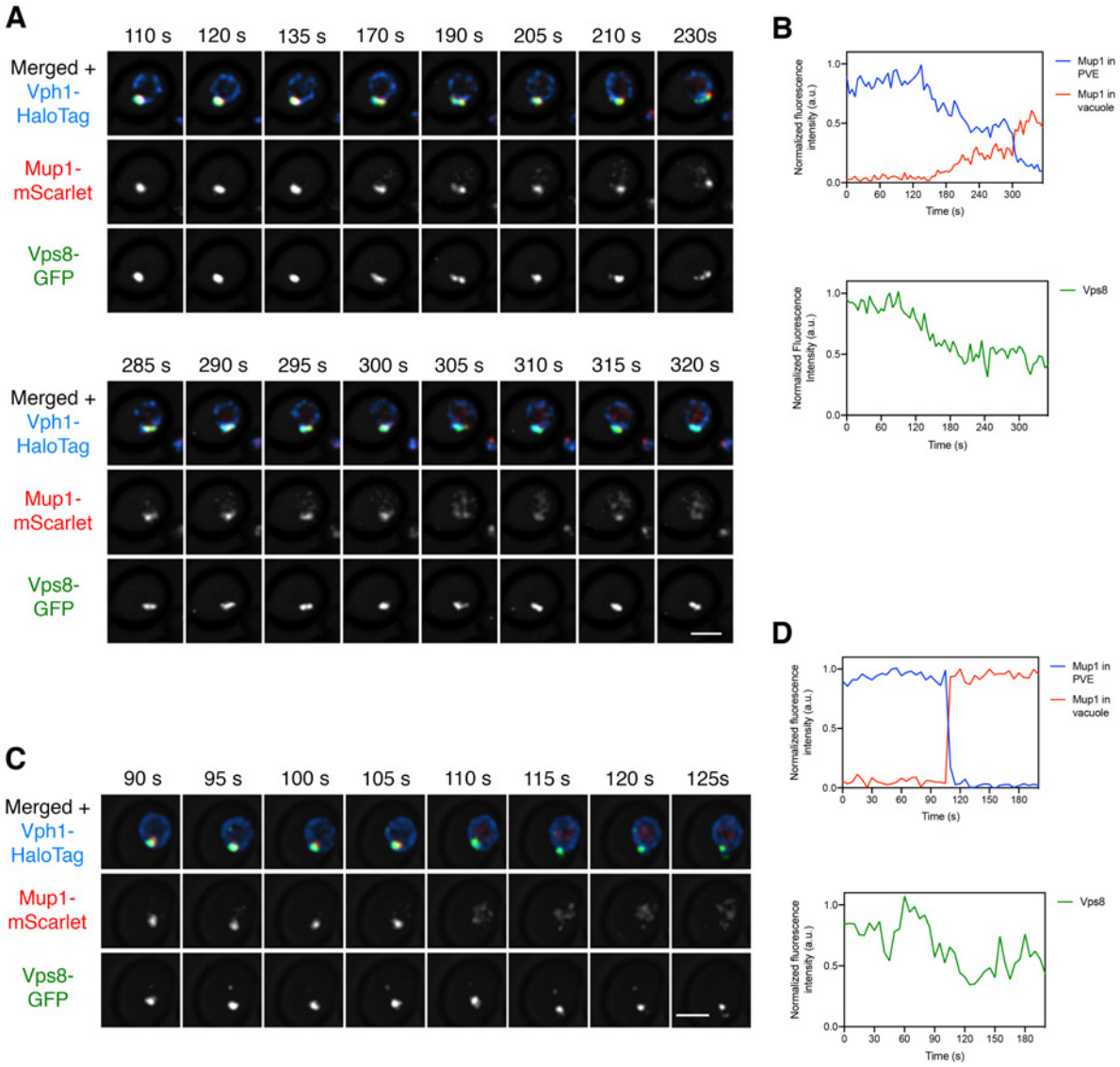

721 **Figure 8.** Visualizing transfer of Mup1 from PVE compartments to the vacuole. (**A)** Movement of
722 Mup1 from a PVE compartment to the vacuole. A strain expressing the vacuolar membrane
723 marker Vph1-HaloTag, the PVE marker Vps8-GFP, and Mup1-mScarlet was grown to mid-log
724 phase in NSD lacking methionine, attached to a confocal dish, and exposed to NSD containing
725 methionine for 10-15 min to promote internalization of Mup1 to PVE compartments. Prior to
726 imaging, a region that excluded PVE compartments was photobleached by illumination with
727 maximum intensity 561-nm laser light for 5 s. Shown are frames from ***Movie 12***, which illustrates
728 a typical example of kiss-and-run fusion at about 300 s. The top row shows the complete
729 projection, the middle row shows the Mup1-mScarlet fluorescence, and the bottom row shows the
730 Vps8-GFP fluorescence. Scale bar, 2 µm. (**B**) Quantification of (**A**), performed as in ***Figure 7B***.
731 At about 300 s, a significant amount of Mup1 moved from the PVE compartment to the vacuole.
732 (**C**) Example of an unusually large kiss-and-run event. The experiment was performed as in (**A**),

733 and frames are shown from ***Movie 13***. Between the 105-s and 110-s time points, virtually all of
734 the Mup1 moved from the PVE compartment to the vacuole. (**D**) Quantification of (**C**), performed
735 as in ***Figure 7B***.

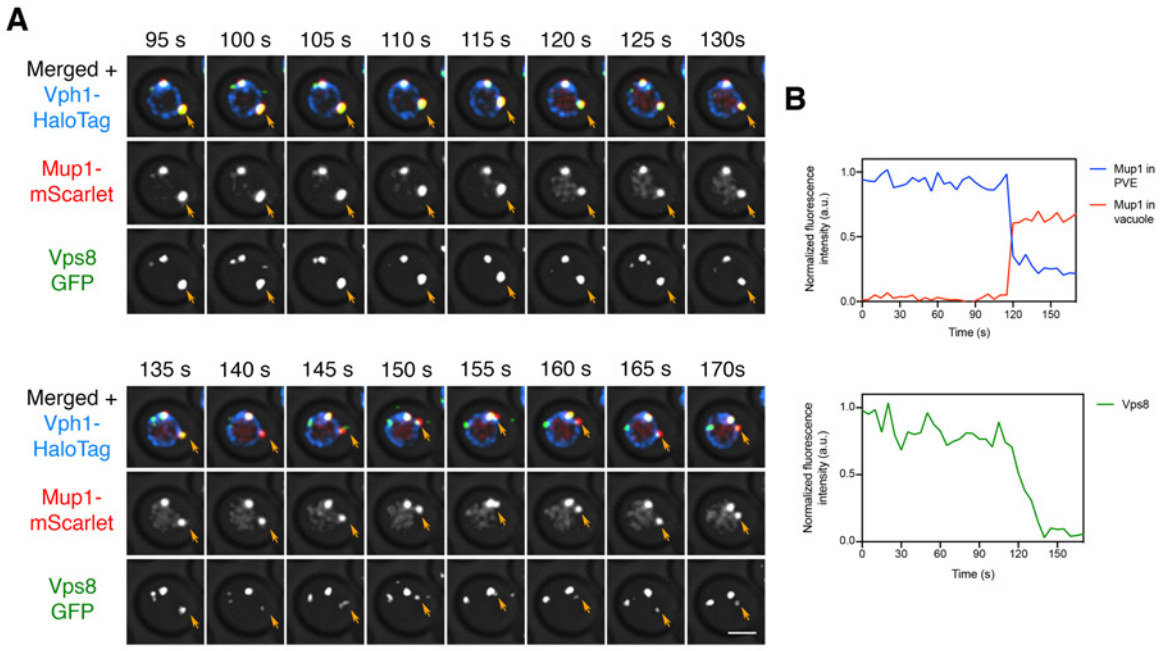

736 **Figure 8—figure supplement 1.** Reduction in Vps8 labeling of a PVE compartment after a large
737 kiss-and-run event. (**A**) Sudden movement of Mup1 from a PVE compartment to the vacuole. The
738 experiment was performed as in ***Figure 8A***, and frames are shown from ***Movie 14***. Orange arrows
739 indicate the PVE compartment that was tracked. (**B**) Quantification of (**A**), performed as in ***Figure***
740 ***7B***. Between the 115-s and 120-s time points, a large fraction of the Mup1 moved from the PVE
741 compartment to the vacuole, and the Vps8-GFP fluorescence began a steep decline.

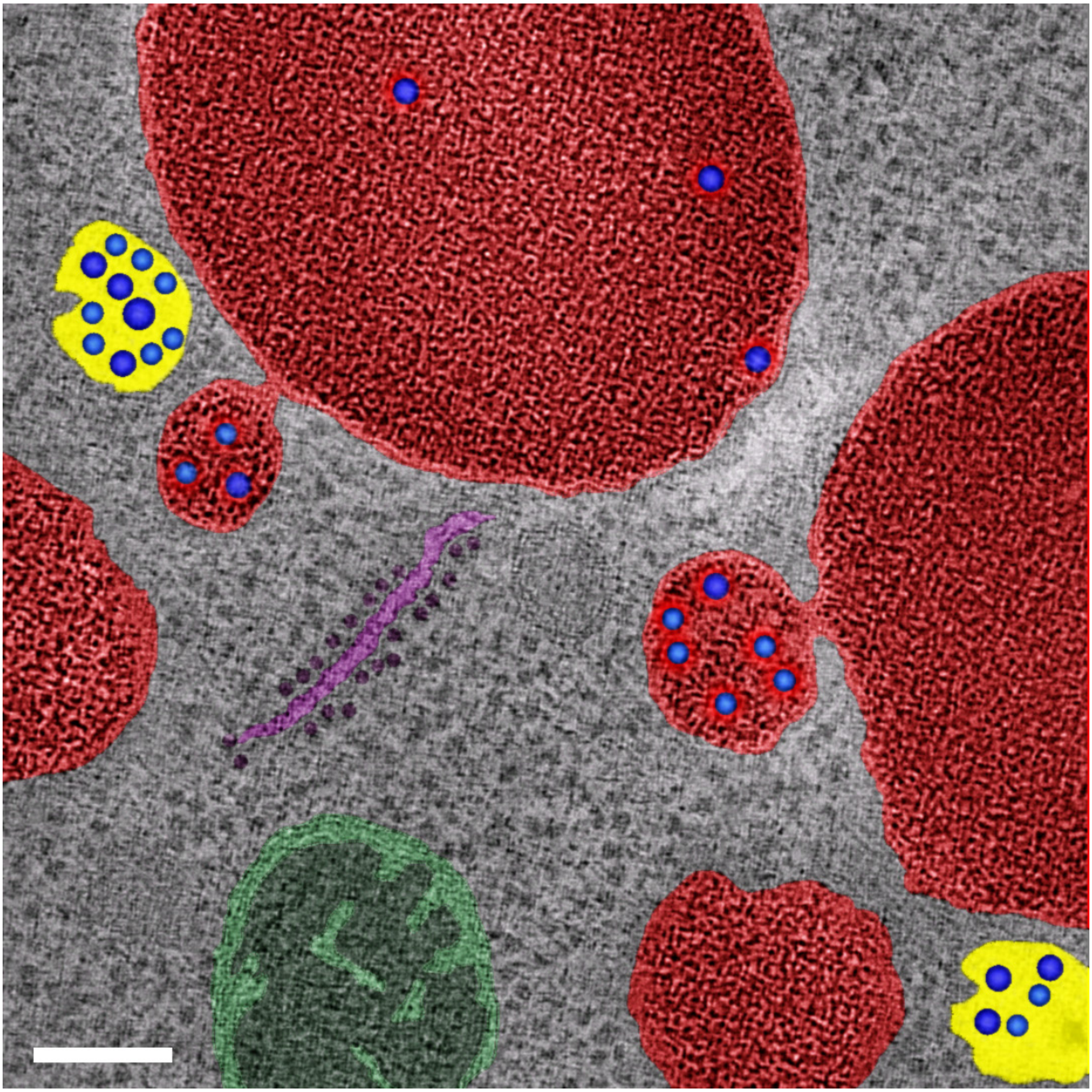

Figure 8—figure supplement 2. Evidence from previously published electron tomography data (McNatt et al., 2007) for partial fusion of PVE compartments with the vacuole. This cover image for the February 2007 issue of Molecular Biology of the Cell (Volume 18, Number 2) was kindly provided by Matt West and Greg Odorizzi, and is reprinted here with permission. It shows electron tomography of vacuoles and associated PVE compartments in *S. cerevisiae*. Non-fused PVE compartments are yellow, vacuoles are red, and PVE compartments with tubular connections to the vacuole are also red to reflect the luminal continuity. Intraluminal vesicles are blue. Also shown are a mitochondrion (green) and a piece of ribosome-studded ER (purple). Scale bar, 100 nm.

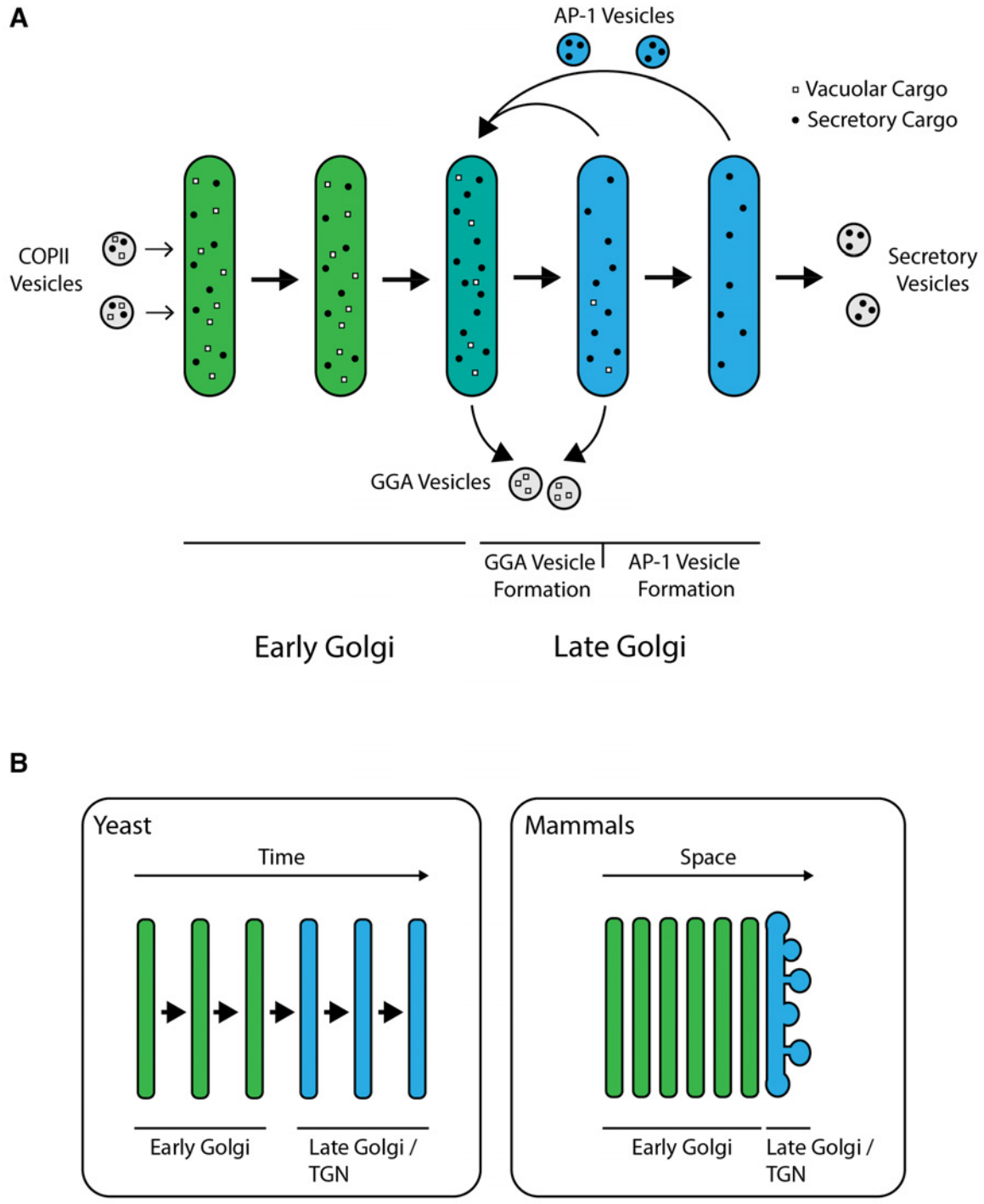

Figure 9. Model for sorting of biosynthetic cargoes in the late Golgi. (**A**) Sequential formation of GGA vesicles and AP-1 vesicles in yeast cells. The thick arrows represent progressive maturation of a Golgi cisterna over time. During the early-to-late Golgi transition of cisternal maturation, GGA adaptors arrive, and GGA vesicles that carry vacuolar cargoes (white squares) begin to form. Subsequently, the AP-1 adaptor arrives, and AP-1 vesicles that recycle resident Golgi proteins

755 (not shown) as well as some secretory cargoes (black dots) begin to form. GGAs depart before
756 AP-1 departs, but the formation phases for GGA vesicles and AP-1 vesicles overlap.
757 (**B**) Comparison of Golgi structures in yeast and mammalian cells. In *S. cerevisiae*, the late Golgi
758 or TGN stage occupies about half of the maturation time, so it is relatively easy to detect
759 sequential arrival times and activities of GGAs and AP-1. In mammalian cells, Golgi cisternae are
760 stacked, with the youngest early Golgi cisterna at the opposite side of a stack from the oldest late
761 Golgi/TGN cisterna. Only the *trans*-most cisterna of a mammalian Golgi stack functions as late
762 Golgi/TGN, but during the lifetime of this cisterna, GGAs and AP-1 may arrive and act sequentially
763 as in yeast.

764 **Movie 1.** Visualizing traffic of the vacuolar cargo from the ER to the vacuole. The cargo expressed
765 in *VPS10* wild-type (WT) and *vps10*Δ strains was imaged by 4D confocal microscopy together
766 with the vacuolar membrane marker Vph1-GFP. Prior to the movie, fluorescence from leaked
767 cargo molecules was bleached by illuminating the vacuole with a 561-nm laser at maximum
768 intensity for 20-30 s. Then SLF was added, and Z-stacks were captured every minute for 60 min.
769 In these average projected Z-stacks, fluorescence data are superimposed on brightfield images
770 of the cells. The top panels show the cargo (magenta) together with Vph1-GFP (green), while the
771 bottom panels show only the cargo. Frames from this movie are shown in ***Figure 2A***. Scale bar,
772 2 μm.

773 **Movie 2.** Visualizing traffic of the vacuolar cargo together with Golgi markers. Cells expressing
774 the cargo together with the early Golgi marker GFP-Vrg4 and the late Golgi marker Sec7-HaloTag
775 were grown to mid-log phase, labeled with JF_{646}, and imaged by 4D confocal microscopy. Prior to
776 imaging, fluorescence from leaked cargo molecules in the vacuole was bleached by illuminating
777 with maximum intensity 561-nm laser power for 20-30 s. SLF was added directly to the dish
778 between the first and second Z-stacks, and then additional Z-stacks were captured every 30 s for
779 29.5 min. In these average projected Z-stacks, fluorescence data are superimposed on brightfield
780 images of the cells. The top panel shows the merged images, and the other panels show the
781 individual fluorescence channels for cargo, Vrg4, and Sec7. Frames from this movie are shown
782 in ***Figure 3A***. Scale bar, 2 μm.

783 **Movie 3.** Visualizing traffic of the vacuolar cargo together with PVE and vacuole markers. Cells
784 expressing the cargo together with the PVE marker Vps8-GFP and the vacuolar membrane
785 marker Vph1-HaloTag were grown to mid-log phase, labeled with JF_{646}, and imaged by 4D
786 confocal microscopy. Prior to imaging, fluorescence from leaked cargo molecules in the vacuole
787 was bleached by illuminating with maximum intensity 561-nm laser power for 20-30 s. SLF was
788 added directly to the dish between the first and second Z-stacks, and then additional Z-stacks
789 were captured every 1 min for 60 min. In these average projected Z-stacks, fluorescence data are
790 superimposed on brightfield images of the cells. The top panel shows the merged images, and
791 the other panels show the individual fluorescence channels for cargo, Vps8, and Vph1. Frames
792 from this movie are shown in ***Figure 3B***. Scale bar, 2 μm.

793 **Movie 4.** Visualizing traffic of the vacuolar cargo during Golgi maturation. Cells expressing the
794 cargo together with the early Golgi marker GFP-Vrg4 and the late Golgi marker Sec7-HaloTag
795 were grown to mid-log phase, labeled with JF_{646}, and imaged by 4D confocal microscopy. SLF
796 was added 1-3 min before imaging. In these average projected Z-stacks, fluorescence data are
797 superimposed on brightfield images of the cells. The top panel shows the complete projection,
798 the second panel shows an edited projection that includes only the cisterna being tracked, and
799 the other panels show the individual fluorescence channels from the edited projection. Frames
800 from this movie are shown in ***Figure 4A***. Scale bar, 2 μm.

801 **Movie 5.** Visualizing traffic of the vacuolar cargo during Golgi maturation in a strain lacking Vps10.
802 The procedure was as in ***Movie 4*** except that a *vps10*Δ strain was used. Frames from this movie
803 are shown in ***Figure 4D***. Scale bar, 2 μm.

804 **Movie 6.** Visualizing the dynamics of the GGA and AP-1 clathrin adaptors during Golgi
805 maturation. Cells expressing the GGA protein Gga2-HaloTag, the AP-1 subunit Apl2-GFP, and
806 the late Golgi marker Sec7-mScarlet were grown to mid-log phase, labeled with JF_{646}, and imaged
807 by 4D confocal microscopy. In these average projected Z-stacks, fluorescence data are
808 superimposed on brightfield images of the cells. The top panel shows the complete projection,
809 the second panel shows an edited projection that includes only the cisterna being tracked, and
810 the other panels show the individual fluorescence channels from the edited projection. Two
811 maturation events are highlighted. Frames from this movie are shown in ***Figure 5A***. Scale bar,
812 2 μm.

813 **Movie 7.** Visualizing the vacuolar cargo together with the GGA clathrin adaptor. Cells expressing
814 the cargo together with the early Golgi marker GFP-Vrg4 and the GGA protein Gga2-HaloTag
815 were grown to mid-log phase, labeled with JF_{646}, and imaged by 4D confocal microscopy. SLF
816 was added 1-3 min before imaging. In these average projected Z-stacks, fluorescence data are
817 superimposed on brightfield images of the cells. The top panel shows the complete projection,
818 the second panel shows an edited projection that includes only the cisterna being tracked, and
819 the other panels show the individual fluorescence channels from the edited projection. Frames
820 from this movie are shown in ***Figure 5C***. Scale bar, 2 μm.

821 **Movie 8.** Visualizing traffic of the vacuolar cargo during Golgi maturation in a strain lacking AP-1.
822 The procedure was as in ***Movie 4*** except that an *apl4*Δ strain was used. Frames from this movie
823 are shown in ***Figure 6A***. Scale bar, 2 μm.

824 **Movie 9.** Visualizing traffic of the vacuolar cargo during Golgi maturation in a strain lacking GGAs.
825 The procedure was as in ***Movie 4*** except that an *gga1*Δ *gga2*Δ strain was used. Frames from this
826 movie are shown in ***Figure 6D***. Scale bar, 2 μm.

827 **Movie 10.** Visualizing gradual kiss-and-run movement of the vacuolar cargo from a PVE
828 compartment to the vacuole. Cells expressing the cargo together with the vacuolar membrane
829 marker Vph1-HaloTag and the PVE marker Vps8-GFP were grown to mid-log phase, attached to
830 a confocal dish, and treated with SLF for 10-15 min to enable the cargo to reach PVE
831 compartments. Prior to imaging, a region that excluded PVE compartments was photobleached
832 by illumination with maximum intensity 561-nm laser light for 40 s. The top panel shows the
833 complete projection, the middle panel shows the cargo fluorescence, and the bottom panel shows
834 the Vps8-GFP fluorescence. Frames from this movie are shown in ***Figure 7A***. Scale bar, 2 μm.

835 **Movie 11.** Visualizing a large kiss-and-run movement of the vacuolar cargo from a PVE
836 compartment to the vacuole. The procedure was as in ***Movie 10***. Frames from this movie are
837 shown in ***Figure 7C***. Scale bar, 2 μm.

838 **Movie 12.** Visualizing kiss-and-run movement of Mup1 from a PVE compartment to the vacuole.
839 Cells expressing the vacuolar membrane marker Vph1-HaloTag, the PVE marker Vps8-GFP, and
840 Mup1-mScarlet were grown to mid-log phase in NSD lacking methionine, attached to a confocal
841 dish, and exposed to NSD containing methionine for 10-15 min to promote internalization of Mup1
842 to PVE compartments. Prior to imaging, a region that excluded PVE compartments was
843 photobleached by illumination with maximum intensity 561-nm laser light for 5 s. The top panel
844 shows the complete projection, the middle panel shows the Mup1-mScarlet fluorescence, and the
845 bottom panel shows the Vps8-GFP fluorescence. Frames from this movie are shown in ***Figure***
846 ***8A***. Scale bar, 2 μm.

847 **Movie 13.** Visualizing a large kiss-and-run movement of Mup1 from a PVE compartment to the
848 vacuole. The procedure was as in ***Movie 12***. Frames from this movie are shown in ***Figure 8C***.
849 Scale bar, 2 μm.

850 **Movie 14.** Reduction in size of a PVE compartment after a large kiss-and-run fusion event. The
851 procedure was as in ***Movie 12***. Frames from this movie are shown in ***Figure 8—figure***
852 ***supplement 1A***. Scale bar, 2 μm.

853

Purpose	Amplifies	Primers
PDR1 deletion	kanMX resistance cassette	5'-CAGCCAAGAATATACAGAAAAGAATCCAAGAAACTGGAAGCGTACGCTGCAGGTCGAC-3' 5'-GGAAGTTTTTGAGAACTTTTATCTATACAAACGTATACGTATCGATGAATTCGAGCTCG-3'
PDR3 deletion	Nourseothricin resistance cassette	5'-ATCAGCAGTTTTATTAATTTTTTCTTATTGCGTGACCGCACGTACGCTGCAGGTCGAC-3' 5'-TACTATGGTTATGCTCTGCTTCCCTATTTTCTTTGCGTTTATCGATGAATTCGAGCTCG-3'
GGA1 deletion	Hygromycin resistance cassette	5'-AGTCACTACTTCAAGTATAACCCAGACAAGAGTCTTTTAAATAGCTTGCCTTGTCCCCGC-3' 5'-ATGGCATCTACTTTTTTTTCAACTTCTCTACCGAATTTGACGTTTTCGACACTGGATGGC-3'
VPS10 deletion	*VPS10* 5' upstream	5'-CCCAAACTAAAAAGTATCCGCCTGT-3' 5'-GACAAGGCAAGCTAACGTGTGATGACTACTGGACACT-3'
	VPS10 3' downstream	5'-GCCATCCAGTGTCGAAGAGATTACTTTACATAGAGTAGATAATTCCATATACTTTTCATA -3' 5'-AATGAAGTACTATAAATATTAAAGTACGTTAGTAGTTTATTTCTCTTCGG-3'
	Hygromycin resistance cassette	5'-TCATCACACGTTAGCTTGCCTTGTCCCCGC-3' 5'-TGTAAAGTAATCTCTTCGACACTGGATGGCGG-3'
APM3 deletion	*APM3* 5' upstream	5'-AGGGGTAGAAGTCGCTGATTGAT-3' 5'-GGGCCTCCATGTCCTATTTTGGTTGGGTTGGTAAGGTTTACAG-3'
	APM3 3' downstream	5'-GCTGGTCGCTATACTGTTATATGTGTACTTGAAATTCCATGCGAAACTAAA-3' 5'-TGCGGAAGTCTTCCCTAAGACG-3'
	Hygromycin resistance cassette	5'-CAACCAAAATAGGACATGGAGGCCCAGAATACCC-3' 5'-TCAAGTACACATATAACAGTATAGCGACCAGCATTCACA-3'
APL4 deletion	*APL4* 5' upstream	5'-ATGTATATAATTCCGGAAGTGTGGTCCT-3' 5'-GACAAGGCAAGCTTATGGTGTTCAGGTCTTTCTCGTTGCT-3'
	APL4 3' downstream	5'-CCATCCAGTGTCGAAAAATGCCTTTAAAATTACAGAACATAACATGATTAATGAC-3' 5'-GAATTCTGGTCCAAGGCAATTCTATATTTGAT-3'
	Hygromycin resistance cassette	5'-CCTGAACACCATAAGCTTGCCTTGTCCCCG-3' 5'-TTTTAAAGGCATTTTTCGACACTGGATGGCGG-3'
GGA2 deletion	*GGA2* 5' upstream	5'-GATTTCTACAGTCTTTCTGATGGGTTCTTGG-3' 5'-ACGATATTCTTAGACATGATGCAGTATCACGATTAGCAAT-3'
	GGA2 3' downstream	5'-AATCTTGGCTTAATCCTCTGGCGTTTCTTATCAATCCTTTCT-3' 5'-TCTTCCTTTGAAGAAAATTCGTCCTCATCT-3'
	K. lactis LEU2	5'-AATCGTGATACTGCATCATGTCTAAGAATATCGTTGTCCTACCGG-3' 5'-GAAACGCCAGAGGATTAAGCCAAGATTTCCTTGACAGCC-3'
Integration at TRP1	*TRP1* locus	5'-GTGTACTTTGCAGTTATGACG-3' 5'-AGTCAACCCCCTGCGATGTATATTTTCCTG-3'

854 **Table 1.** Primers used in this study.

References

Adell, M.A.Y., S.M. Migliano, S. Upadhyayula, Y.S. Bykov, S. Sprenger, M. Pakdel, G.F. Vogel, G. Jih, W. Skillern, R. Behrouzi, M. Babst, O. Schmidt, M.W. Hess, J.A.G. Briggs, T. Kirchhausen, and D. Teis. 2017. Recruitment dynamics of ESCRT-III and Vps4 to endosomes and implications for reverse membrane budding. *eLife*. 6:e31652.

Arlt, H., K. Auffarth, R. Kurre, D. Lisse, J. Piehler, and C. Ungermann. 2015. Spatiotemporal dynamics of membrane remodeling and fusion proteins during endocytic transport. *Mol. Biol. Cell*. 26:1357-1370.

Balderhaar, H.J., and C. Ungermann. 2013. CORVET and HOPS tethering copmplexes – coordinators of endosome and lysosome fusion. *J. Cell Sci.* 126:1307-1316.

Barrero, J.J., E. Papanikou, J.C. Casler, K.J. Day, and B.S. Glick. 2016. An improved reversibly dimerizing mutant of the FK506-binding protein FKBP. *Cell. Logist.* 6:e1204848.

Bevis, B.J., A.T. Hammond, C.A. Reinke, and B.S. Glick. 2002. *De novo* formation of transitional ER sites and Golgi structures in *Pichia pastoris*. *Nat. Cell Biol.* 4:750-756.

Black, M.W., and H.R. Pelham. 2000. A selective transport route from Golgi to late endosomes that requires the yeast GGA proteins. *J. Cell Biol.* 151:587-600.

Bowers, K., and T.H. Stevens. 2005. Protein transport from the late Golgi to the vacuole in the yeast *Saccharomyces cerevisiae*. *Biochim. Biophys. Acta*. 1744:438-454.

Bright, N.A., L.J. Davis, and J.P. Luzio. 2016. Endolysosomes are the principal intracellular sites of acid hydrolase activity. *Curr. Biol.* 26:2233-2245.

Bright, N.A., M.J. Gratian, and J.P. Luzio. 2005. Endocytic delivery to lysosomes mediated by concurrent fusion and kissing events in living cells. *Curr. Biol.* 15:360-365.

Casler, J.C., and B.S. Glick. 2019. Visualizing secretory cargo transport in budding yeast. *Curr. Protoc. Cell Biol.* 83:e80.

Casler, J.C., E. Papanikou, J.J. Barrero, and B.S. Glick. 2019. Maturation-driven transport and AP-1–dependent recycling of a secretory cargo in the Golgi. *J. Cell Biol.* 218:1582-1601.

Chen, Y., D.C. Gershlick, S.Y. Park, and J.S. Bonifacino. 2017. Segregation in the Golgi complex precedes export of endolysosomal proteins in distinct transport carriers. *J. Cell Biol.* 216:4141-4151.

Conibear, E., and T.H. Stevens. 1998. Multiple sorting pathways between the late Golgi and the vacuole in yeast. *Biochim. Biophys. Acta*. 1404:211-230.

Coorey, N.V.C., J.H. Matthews, D.S. Bellows, and P.H. Atkinson. 2015. Pleiotropic drug-resistance attenuated genomic library improves elucidation of drug mechanisms. *Mol. Biosyst.* 11:3129-3136.

Cowles, C.R., G. Odorizzi, G.S. Payne, and S.D. Emr. 1997. The AP-3 adaptor complex is essential for cargo-selective transport to the yeast vacuole. *Cell*. 91:109-118.

Daboussi, L., G. Costaguta, R. Ghukasyan, and G.S. Payne. 2017. Conserved role for Gga proteins in phosphatidylinositol 4-kinase localization to the *trans*-Golgi network. *Proc. Natl Acad. Sci. USA*. 114:3433-3438.

Daboussi, L., G. Costaguta, and G.S. Payne. 2012. Phosphoinositide-mediated clathrin adaptor progression at the *trans*-Golgi network. *Nat. Cell Biol.* 14:239-248.

Day, K.J., J.C. Casler, and B.S. Glick. 2018. Budding yeast has a minimal endomembrane system. *Dev. Cell*. 44:56-72.

Day, K.J., P.J. La Rivière, T. Chandler, V.P. Bindokas, N.J. Ferrier, and B.S. Glick. 2017. Improved deconvolution of very weak confocal signals. *F1000Res.* 6:787.

Day, K.J., E. Papanikou, and B.S. Glick. 2016. 4D confocal imaging of yeast organelles. *Methods Mol. Biol.* 1496:1-11.

De Matteis, M.A., and A. Luini. 2008. Exiting the Golgi complex. *Nat. Rev. Mol. Cell Biol.* 9:273-284.

Dell'Angelica, E.C., R. Puertollano, C. Mullins, R.C. Aguilar, J.D. Vargas, L.M. Hartnell, and J.S. Bonifacino. 2000. GGAs: a family of ADP ribosylation factor-binding proteins related to adaptors and associated with the Golgi complex. *J. Cell Biol.* 149:81-94.

Endrizzi, J.A., K. Breddam, and S.J. Remington. 1994. 2.8-Å structure of yeast serine carboxypeptidase. *Biochemistry*. 33:11106-11120.

Feyder, S., J.O. De Craene, S. Bär, D.L. Bertazzi, and S. Friant. 2015. Membrane trafficking in the yeast *Saccharomyces cerevisiae* model. *Int. J. Mol. Sci.* 16:1509-1525.

Fitzgerald, I., and B.S. Glick. 2014. Secretion of a foreign protein from budding yeasts is enhanced by cotranslational translocation and by suppression of vacuolar targeting. *Microb. Cell Fact.* 13:125.

Goldstein, A.L., and J.H. McCusker. 1999. Three new dominant drug resistance cassettes for gene disruption in *Saccharomyces cerevisiae*. *Yeast*. 15:1541-1553.

Griffiths, G., and K. Simons. 1986. The *trans* Golgi network: sorting at the exit site of the Golgi complex. *Science*. 234:438-443.

Grimm, J.B., B.P. English, J. Chen, J.P. Slaughter, Z. Zhang, A. Revyakin, R. Patel, J.J. Macklin, D. Normanno, R.H. Singer, T. Lionnet, and L.D. Lavis. 2015. A general method to improve fluorophores for live-cell and single-molecule microscopy. *Nat. Methods*. 12:244-250.

Hammond, A.T., and B.S. Glick. 2000. Raising the speed limits for 4D fluorescence microscopy. *Traffic*. 1:935-940.

Hecht, K.A., A.F. O''Donnell, and J.L. Brodsky. 2014. The proteolytic landscape of the yeast vacuole. *Cell. Logist.* 4:e28023.

Henne, W.M., N.J. Buchkovich, and S.D. Emr. 2011. The ESCRT pathway. *Dev. Cell*. 21:77-91.

Hinners, I., and S.A. Tooze. 2003. Changing directions: clathrin-mediated transport between the Golgi and endosomes. *J. Cell Sci.* 116:763-771.

Hirst, J., M.R. Lindsay, and M.S. Robinson. 2001. GGAs: roles of the different domains and comparison with AP-1 and clathrin. *Mol. Biol. Cell*. 12:3573-3588.

Hirst, J., W.W.Y. Lui, N.A. Bright, N. Totty, M.N.J. Seaman, and M.S. Robinson. 2000. A family of proteins with γ-adaptin and VHS domains that facilitate trafficking between the TGN and the vacuole/lysosome. *J. Cell Biol.* 149:67-79.

Ishii, M., Y. Suda, H. Kurokawa, and A. Nakano. 2016. COPI is essential for Golgi cisternal maturation and dynamics. *J. Cell Sci.* 129:3251-3261.

Johnson, L.M., V.A. Bankaitis, and S.D. Emr. 1987. Distinct sequence determinants direct intracellular sorting and modification of a yeast vacuolar protease. *Cell*. 48:875-885.

Johnson, N., and B.S. Glick. 2019. 4D microscopy of yeast. *J. Vis. Exp.*

Kaiser, C.A., R.E. Gimeno, and D.A. Shaywitz. 1997. Protein secretion, membrane biogenesis, and endocytosis. *In* The Molecular and Cellular Biology of the Yeast *Saccharomyces*. Vol. 3. J.R. Pringle, J.R. Broach, and E.W. Jones, editors. Cold Spring Harbor Laboratory Press. 91-227.

Kim, J.J., Z. Lipatova, and N. Segev. 2016. Regulation of Golgi cisternal progression by Ypt/Rab GTPases. *Dev. Cell*. 36:440-452.

Kunz, J., U. Schneider, M. Deuter-Reinhard, N.R. Movva, and M.N. Hall. 1993. Target of rapamycin in yeast, TOR2, is an essential phosphatidylinositol kinase homolog required for G1 progression. *Cell*. 73:585-596.

Kurokawa, K., M. Ishii, Y. Suda, A. Ichihara, and A. Nakano. 2013. Live cell visualization of Golgi membrane dynamics by super-resolution confocal live imaging microscopy. *Methods Cell Biol.* 118:235-242.

Kurokawa, K., O. Osakada, T. Kodijani, M. Waga, Y. Suda, H. Asakawa, T. Haraguchi, and A. Nakano. 2019. Visualization of secretory cargo transport within the Golgi apparatus. *J. Cell Biol.* 218:1602-1618.

Ladinsky, M.S., D.N. Mastronarde, J.R. McIntosh, K.E. Howell, and L.A. Staehelin. 1999. Golgi structure in three dimensions: functional insights from the normal rat kidney cell. *J. Cell Biol.* 144:1135-1149.

Lin, C.H., J.A. MacGurn, T. Chu, C.J. Stefan, and S.D. Emr. 2008. Arrestin-related ubiquitin-ligase adaptors regulate endocytosis and protein turnover at the cell surface. *Cell*. 135:714-725.

Lippincott-Schwartz, J., T.H. Roberts, and K. Hirschberg. 2000. Secretory protein trafficking and organelle dynamics in living cells. *Annu. Rev. Cell Dev. Biol.* 16:557-589.

Liu, K., K. Surendhran, S.F. Nothwehr, and T.R. Graham. 2008. P4-ATPase requirement for AP-1/clathrin function in protein transport from the *trans*-Golgi network and early endosomes. *Mol. Biol. Cell*. 19:3526-3535.

Llinares, E., A.O. Barry, and B. André. 2015. The AP-3 adaptor complex mediates sorting of yeast and mammalian PQ-loop-family basic amino acid transporters to the vacuolar/lysosomal membrane. *Sci. Rep.* 5:16665.

Losev, E., C.A. Reinke, J. Jellen, D.E. Strongin, B.J. Bevis, and B.S. Glick. 2006. Golgi maturation visualized in living yeast. *Nature*. 441:1002-1006.

Ma, M., and C.G. Burd. 2020. Retrograde trafficking and plasma membrane recycling pathways of the budding yeast *Saccharomyces cerevisiae*. *Traffic*. 21:45-59.

MacDonald, C., N.J. Buchkovich, D.K. Stringer, S.D. Emr, and R.C. Piper. 2012. *Cargo ubiquitination is essential for multivesicular body intralumenal vesicle formation*. 13:331-338.

Marcusson, E.G., B.F. Horazdovsky, J. Lin Cereghino, E. Gharakhanian, and S.D. Emr. 1994. The sorting receptor for yeast vacuolar carboxypeptidase Y is encoded by the *VPS10* gene. *Cell*. 77:579-586.

Matsuura-Tokita, K., M. Takeuchi, A. Ichihara, K. Mikuriya, and A. Nakano. 2006. Live imaging of yeast Golgi cisternal maturation. *Nature*. 441:1007-1010.

McDonold, C.M., and J.C. Fromme. 2014. Four GTPases differentially regulate the Sec7 Arf-GEF to direct traffic at the *trans*-Golgi network. *Dev. Cell*. 30:759-767.

McNatt, M.W., I. McKittrick, M. West, and G. Odorizzi. 2007. Direct binding to Rsp5 mediates ubiquitin-independent sorting of Sna3 via the multivesicular body pathway. *Mol. Biol. Cell*. 18:697-706.

Menant, A., R. Barbey, and D. Thomas. 2006. Substrate-mediated remodeling of methioning transport by multiple ubiquitin-dependent mechanisms in yeast cells. *EMBO J.* 25:4436-4447.

Mogelsvang, S., B.J. Marsh, M.S. Ladinsky, and K.E. Howell. 2004. Predicting function from structure: 3D structure studies of the mammalian Golgi complex. *Traffic*. 5:338-345.

Myers, M.D., and G.S. Payne. 2013. Clathrin, adaptors and disease: insights from the yeast *Saccharomyces cerevisiae*. *Front. Biosci.* 18:862-891.

Novick, P., C. Field, and R. Schekman. 1980. Identification of 23 complementation groups required for post-translational events in the yeast secretory pathway. *Cell*. 21:205-215.

Odorizzi, G., C.R. Cowles, and S.D. Emr. 1998. The AP-3 complex: a coat of many colors. *Trends Cell Biol.* 8:282-288.

Pantazopoulou, A., and B.S. Glick. 2019. Membrane traffic pathways define the transitions in Golgi maturation. *Front. Cell Dev. Biol.* Submitted (invited review).

Papanikou, E., K.J. Day, J. Austin, 2nd, and B.S. Glick. 2015. COPI selectively drives maturation of the early Golgi. *eLife*. 4:e13232.

Pelham, H.R.B. 2002. Insights from yeast endosomes. *Curr. Opin. Cell Biol.* 14:454-462.

Preuss, D., J. Mulholland, A. Franzusoff, N. Segev, and D. Botstein. 1992. Characterization of the *Saccharomyces* Golgi complex through the cell cycle by immunoelectron microscopy. *Mol. Biol. Cell*. 3:789-803.

Rivera-Molina, F.E., and P.J. Novick. 2009. A Rab GAP cascade defines the boundary between two Rab GTPases on the secretory pathway. *Proc. Natl. Acad. Sci. USA*. 106:14408-14413.

Rossanese, O.W., J. Soderholm, B.J. Bevis, I.B. Sears, J. O'Connor, E.K. Williamson, and B.S. Glick. 1999. Golgi structure correlates with transitional endoplasmic reticulum organization in *Pichia pastoris* and *Saccharomyces cerevisiae*. *J. Cell Biol.* 145:69-81.

Rothstein, R. 1991. Targeting, disruption, replacement, and allele rescue: integrative DNA transformation in yeast. *Methods Enzymol.* 194:281-301.

Schneider, C.A., W.S. Rasband, and K.W. Eliceiri. 2012. NIH Image to ImageJ: 25 years of image analysis. *Nat. Methods*. 9:671-675.

Schüller, C., Y.M. Mamnun, H. Wolfger, N. Rockwell, J. Thorner, and K. Kuchler. 2007. Membrane-active compounds activate the transcription factors Pdr1 and Pdr3 connecting pleiotropic drug resistance and membrane lipid homeostasis in *Saccharomyces cerevisiae*. *Mol. Biol. Cell*. 18:4932-4944.

Spang, A. 2015. The road not taken: less traveled roads from the TGN to the plasma membrane. *Membranes (Basel)*. 5:84-98.

Stevens, T., B. Esmon, and R. Schekman. 1982. Early stages in the yeast secretory pathway are required for transport of carboxypeptidase Y to the vacuole. *Cell*. 30:439-448.

Suda, Y., K. Kurokawa, R. Hirata, and A. Nakano. 2013. Rab GAP cascade regulates dynamics of Ypt6 in the Golgi traffic. *Proc. Natl. Acad. Sci. USA*. 110:18976-18981.

Thomas, L.L., and J.C. Fromme. 2020. Extensive GTPase crosstalk regulates Golgi trafficking and maturation. *Curr. Opin. Cell Biol.* 65:1-7.

Tojima, T., Y. Suda, M. Ishii, K. Kurokawa, and A. Nakano. 2019. Spatiotemporal dissection of the *trans*-Golgi network in budding yeast. *J. Cell Sci.* 132: jcs231159.

Valdivia, R.H., D. Baggott, J.S. Chuang, and R. Schekman. 2002. The yeast clathrin adaptor protein complex 1 is required for the efficient retention of a subset of late Golgi membrane proteins. *Dev. Cell*. 2:283-294.

Valls, L.A., C.P. Hunter, J.H. Rothman, and T.H. Stevens. 1987. Protein sorting in yeast: the localization determinant of yeast vacuolar carboxypeptidase Y resides in the propeptide. *Cell*. 48:887-897.

Valls, L.A., J.R. Winther, and T.H. Stevens. 1990. Yeast carboxypeptidase Y vacuolar targeting signal is defined by four propeptide amino acids. *J. Cell Biol.* 111:361-368.

Vida, T.A., G. Huyer, and S.D. Emr. 1993. Yeast vacuolar proenzymes are sorted in the late Golgi complex and transported to the vacuole via a prevacuolar endosome-like compartment. *J. Cell Biol.* 121:1245-1256.

Wach, A., A. Brachat, R. Pohlmann, and P. Philippsen. 1994. New heterologous modules for classical or PCR-based gene disruptions in *Saccharomyces cerevisiae*. *Yeast*. 10:1793-1808.

Wooding, S., and H.R.B. Pelham. 1998. The dynamics of Golgi protein traffic visualized in living yeast cells. *Mol. Biol. Cell*. 9:2667-2680.

Yin, Y., M.R. Garcia, A.J. Novak, A.M. Saunders, R.S. Ank, A.S. Nam, and L.W. Fisher. 2018. Surf4 (Erv29p) binds amino-terminal tripeptide motifs of soluble cargo proteins with different affinities, enabling prioritization of their exit from the endoplasmic reticulum. *PLoS Biol.* 16:e2005140.

Zhdankina, O., N.L. Strand, J.M. Redmond, and A.L. Boman. 2001. Yeast GGA proteins interact with GTP-bound Arf and facilitate transport through the Golgi. *Yeast*. 18:1-18.